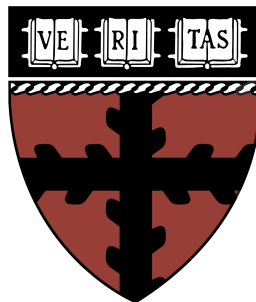
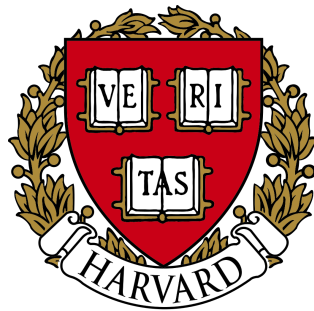


Using the Velocity Anisotropy Technique to Investigate Interstellar Magnetohydrodynamic Turbulence

Missy McIntosh

Advised by Blakesley Burkhart,
Astronomy Department, Harvard University, Cambridge, MA 02138

A thesis presented to the Department of Astronomy and the Department of Electrical
Engineering of Harvard College in partial fulfillment of the requirements for a joint degree
of Bachelor of Arts



Acknowledgements

I would like to thank my adviser, Blakesley Burkhart, for her considerable patience in guiding my efforts on this thesis. I would also like to thank Dave Charbonneau who compelled me to write this thesis when I might have delayed. Finally, I would like to thank my external reviewers, Chat Hull and Michael Dunham, for their time and attention to detail.

*Big whorls have little whorls,
which feed on their velocity;
And little whorls have lesser whorls,
And so on to viscosity.
- L. F. Richardson, 1922.*

Abstract

Magnetohydrodynamic (MHD) turbulence in the interstellar medium (ISM) influences star formation and subsequently the way our Galaxy evolves. Direct observations of magnetic fields for studying MHD turbulence can be difficult and costly to obtain; as an alternative, we explore a technique called velocity anisotropy to probe MHD turbulence. We apply the velocity anisotropy technique (VAT) in CO radiative transfer MHD simulations for the first time and also to non-synthetic observations for the first time. We find that for optically thin radiative transfer simulations, the sub-Alfvénic and super-Alfvénic regimes are indistinguishable. For the optically thick case the regimes were distinguishable. We then apply the VAT to ^{12}CO and ^{13}CO emission line observations of the Taurus Molecular Cloud, and compare results with that of a principal component analysis (PCA) technique detailed in Heyer & Brunt (2011). We find that increased velocity anisotropy did not correspond to regions of lower gas column density/visual extinction as it did when analyzed with PCA, though this may be due to the selection of region size. We also found ^{12}CO emission to show more velocity anisotropy than ^{13}CO emission, in agreement with the PCA analysis. As a preface to and to supply context for the VAT and its usefulness, we first overview the ISM, turbulence, MHD turbulence in the ISM, and the interstellar magnetic field. We discuss the challenges of observing magnetic fields and the need for methods like VAT to study these fields, MHD turbulence, and the way our Galaxy evolves.

Contents

Abstract	4
1 Introduction	7
1.1 The Interstellar Medium	8
1.2 Turbulence Theory	10
1.3 Interstellar Magnetohydrodynamic Turbulence	19
1.4 Observing MHD Turbulence in the ISM	23
1.5 The Interstellar Magnetic Field	26
1.6 The Challenges of Observing Magnetic Fields	28
1.7 Turbulence Statistics as Alternatives	35
1.7.1 Velocity Anisotropy Technique (VAT)	36
1.7.2 Principal Component Analysis (PCA)	39
2 The Scope of this Thesis	41
3 The Data	42
3.1 Simulating MHD Turbulence with Radiative Transfer	42
3.2 Taurus Molecular Cloud Emission Data	45
4 Method of Applying VAT	50

5	Results	51
6	Conclusion	55
	References	58
	Appendix	63

1. Introduction

This thesis is an exploration of a technique called velocity anisotropy (a technique also discussed by Esquivel & Lazarian (2011) and Burkhart et al. (2014)). This technique probes magnetohydrodynamic (MHD) turbulence in the interstellar medium (ISM). MHD turbulence in the ISM is important because of its influence on star formation and subsequent influence on the way our Milky Way evolves (McKee & Ostriker 2007; Elmegreen & Scalo 2004; Falceta-Gonçalves et al. 2014). Current methods of observing interstellar magnetic fields in MHD turbulence are time intensive and costly, so exploring new statistical techniques for measuring MHD turbulence is advantageous. In this thesis we apply the velocity anisotropy technique (VAT) to both compressible MHD simulations including radiative transfer and also observational data for the first time. Understanding the VAT’s ability to describe MHD turbulence is useful as it is an easily computed statistic. Developing and testing techniques such as the VAT allows for more flexibility and potentially better accuracy when describing the ISM throughout our Galaxy (Burkhart 2014).

To provide context for the exploration of MHD turbulence in the ISM, we begin with an overview of the ISM, turbulence theory, MHD turbulence, and interstellar magnetic fields. We discuss the challenges of producing magnetic field observations, motivating the production of statistical techniques like the VAT which can describe magnetic fields in the ISM from indirect observations.

In order to effectively model MHD turbulence a combination of theory, numerical simulations, and observational data with statistical studies is most helpful (Burkhart 2014). We discuss the advantages of numerical simulations and how they are translated to synthetic observations such that they are comparable with observations of the interstellar medium. We apply the VAT to radiative transfer MHD simulations with various Sonic Mach numbers and analyze the resulting trend. We then apply the VAT to emission data for the Taurus

Molecular Cloud, and explain why it is a good target for MHD turbulence studies. We end by briefly comparing the results of the VAT to a principal component analysis (PCA) of MHD turbulence in the Taurus Molecular Cloud as presented by Heyer & Brunt (2011).

1.1. The Interstellar Medium

Permeating our galaxy is the interstellar medium (ISM). It is composed of gaseous hydrogen and helium, with a spritz of heavier elements from the death of stars, some dust grains, cosmic rays, and embedded magnetic fields (Ferrière 2001; Tielens 2005; Vazquez-Semadeni 2012). The ISM contains condensed clouds, larger void-like pockets, shells, and bubbles over a wide range of scales, concentrated mostly in shock fronts near the Galactic plane and spiral arms of our Galaxy (Ferrière 2001; Vazquez-Semadeni 2012).

The gas component of the ISM is $\sim 10^{10} M_{\odot}$ or about $\sim 10 - 15\%$ of the total mass of the Galactic disk (Ferrière 2001; Vazquez-Semadeni 2012). Its contents are mostly hydrogen, accompanied by 10% helium, 0.1% carbon, nitrogen, or oxygen, and tiny amounts of heavier elements (Dyson & Williams 1997). It is also dusty, but with a particle-number ratio of gas to dust of 10^{12} (Dyson & Williams 1997).

We categorize parts of the ISM based on the form of its gas, its temperature, its density, and its ionization fraction (Ferrière 2001; Tielens 2005; Vazquez-Semadeni 2012). The gas can be ionized, neutral atomic, or neutral molecular, and we loosely split the temperatures into cool ($< 10^4$ K), warm ($\sim 10^4$ K), and hot ($\sim 10^6$ K) (Ferrière 2001; Vazquez-Semadeni 2012). We call categories or phases of the ISM cold neutral (CNM), warm neutral (WNM), warm ionized (WIM), hot ionized (HIM), and sometimes distinguish a warm partially ionized phase (Savage & Mathis 1979; McKee & Ostriker 2007; Vazquez-Semadeni 2012).

Thermal instability causes the ISM to separate into different phases— certain tem-

perature and density values are unstable and small deviations from these values will cause runaway heating or cooling in the ISM (Vazquez-Semadeni 2012). The heating or cooling will slow and stop once the ISM reaches stable temperature and density values. These stable values are the aforementioned phases. However, these phases aren’t isolated from their often turbulent surroundings (Vazquez-Semadeni 2012). Turbulence, a mixing phenomenon defined more exactly in Section 1.2, acts against phase separation, pushing the ISM into unstable, in-between phase regimes (Vazquez-Semadeni 2012). These unstable regimes produced by turbulence may consist of up to half of the mass of the ISM (Vazquez-Semadeni 2012).

Commonly studied structures in the ISM include molecular clouds (MCs). In fact, half of ISM’s mass and $\sim 1 - 2\%$ of the interstellar volume is contained in these clumpy, cooler, discrete clumps/clouds (Ferrière 2001). The remaining ISM is warm or hot and is either diffusely spread between these clouds or slightly concentrated in patches, filaments, or structures called bubbles, superbubbles, and loops (Ferrière 2001; Vazquez-Semadeni 2012). The temperature, density, and scale height (the distance for which the density decreases by a factor of e) for these phases and structures are shown in Table 1.

Perhaps the most important role that the ISM plays in our Galaxy is that of forming and recycling stars (Ferrière 2001). Star formation determines the structure and evolution of our Galaxy and yields the materials that make up our planets and ourselves (McKee & Ostriker 2007). After forming, stars can interact with the ISM through supernovae, stellar winds, and ionizing radiation fields (Ferrière 2001). These interactions inject material and energy, causing compression waves and turbulence, and creating structure and ionized regions in the ISM, including nebulae, molecular clouds, HI clouds, HII regions, (super)bubbles, circumstellar disks, and supernova remnants (Ferrière 2001). Figure 1 illustrates some of these objects. The exact role of MHD turbulence in the star formation cycle is an active

Table 1:: Phases of the ISM (Ferrière 2001).

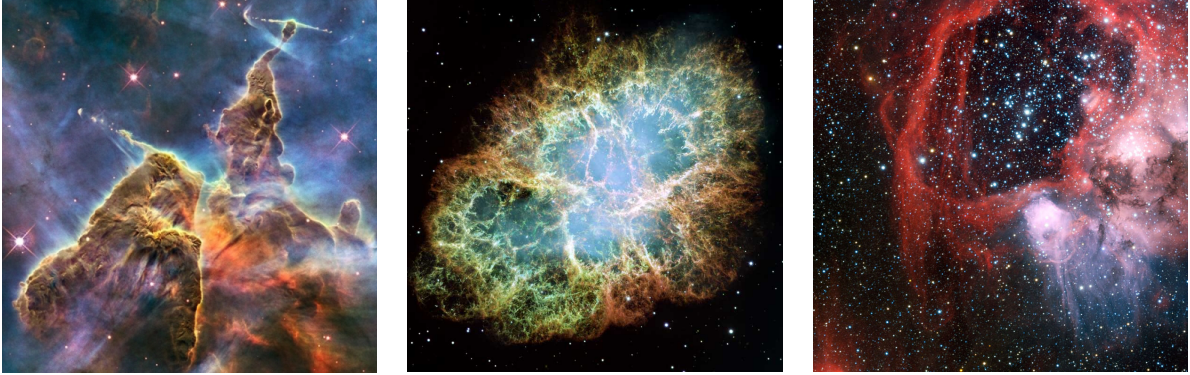
Phase or Structure	Density (atoms cm ⁻³)	Temperature (K)	Scale height (pc)	Fractional Volume (% of ISM)	State of hydrogen
MC	$10^2 - 10^6$	$10 - 29$	80	< 1	molecular
CNM	$20 - 50$	$50 - 100$	$100 - 300$	$1 - 5$	neutral atomic
WNM	$0.2 - 0.5$	$6000 - 10000$	$300 - 400$	$10 - 20$	neutral atomic
WIM	$0.2 - 0.4$	8000	1000	$20 - 50$	ionized
HIM	$10^{-4} - 10^{-2}$	8000	$1000 - 3000$	< 1	ionized
HII	$10^2 - 10^4$	$10^6 - 10^7$	70	$30 - 70$	ionized

area of research, underscoring the importance of developing the VAT and other techniques.

1.2. Turbulence Theory

Turbulence is important in all astrophysics that involve gas dynamics (McKee & Ostriker 2007). This includes large scale ISM structure, like the spiral arms in a galaxy, and smaller scale structure, like compression in molecular cloud formation which leads to star formation (Elmegreen & Scalo 2004). Understanding turbulence, magnetic fields, and structure in the ISM is key to understanding how galaxies evolve to look the way that they do in gas, dust, and stars, and to understand the mechanisms that fuel these evolutionary processes (Elmegreen & Scalo 2004).

In these sections we describe turbulence, its energy cascade, statistics used to describe turbulence such as the Reynolds, Sonic Mach, and Alfvén Mach numbers, the Navier-Stokes equations (which govern turbulent and other fluid flow), magnetohydrodynamic turbulence in the ISM, and outline the turbulence theories developed by Kolmogorov in 1941 and



(a) A molecular cloud in Carina (Hubble Telescope 2013) (b) The Crab Nebula, a planetary nebula (Hubble Image & of Arizona State University 2005) (c) Superbubble LHA 120-N 44 in the Large Magellanic Cloud (Very Large Telescope image 2011)

Fig. 1.—: Images of some structures present in the ISM

Goldreich and Sridhar in 1995.

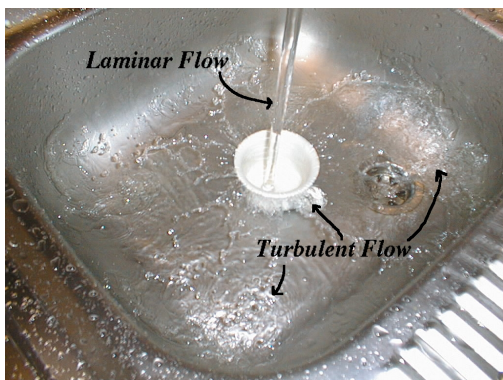
Colloquially, turbulence is used to describe something that is chaotic and random. While it is true that the long term properties of turbulence are unpredictable, turbulence is not actually random (McDonough 2007; Ball 2014; Falceta-Gonçalves et al. 2014). True randomness requires the characteristics of any point to be temporally independent of any other point (Ball 2014). Taking the average of something random results in something uniform, but taking the average of turbulence results in non-uniformity; though turbulence may seem chaotic, it has specific statistical properties that are revealed through temporal and spatial averaging (Ball 2014). Subsequently, turbulence can be studied and modeled in terms of statistical quantities (Falceta-Gonçalves et al. 2014).

More technically, turbulence can be defined as nonlinear fluid motion due to an input of energy over a broad range of correlated spatial and temporal scales (Elmegreen & Scalo 2004). Turbulence can be classified as wave or fluid, compressible or incompressible, and

gravitationally, thermally, or magnetically driven (McDonough 2007). Characteristics of turbulent flows include seemingly random behavior, sensitivity to initial conditions (nonrepeatability), large ranges of length and time scales that satisfy the continuum hypothesis (an approximation that fluids are continuous rather than discrete), mixing motions, dissipation, 3D time dependence, and rotationality (McDonough 2007).

When looking at a turbulent fluid, such as rapids in a river, you would see a churning and tumultuous hierarchy of eddies of all different sizes (Ball 2014). The cause of this churning is kinetic energy which has been somehow injected into the fluid. Energy is not injected on the length and time scale of each eddy in the hierarchy, but is rather injected on a large spatial and temporal scale and then “cascades” (is transferred) down to successively smaller scales, feeding the eddies at each scale along the way (McDonough 2007; Ball 2014; Falceta-Gonçalves et al. 2014). At the smallest scales, the energy exits the cascade as heat from the friction of molecules rubbing together (viscosity), though the bulk of the injected kinetic energy remains at large scales (McDonough 2007; Ballesteros-Paredes et al. 2007; Ball 2014). This means that turbulence does not start out as a hierarchy of eddies, but rather one large swirling motion/eddy/vortex from some local fluid instability (Falceta-Gonçalves et al. 2014). This motion is unstable and fragments into smaller and smaller vortices, until the motions are so small they are damped out by viscosity (Falceta-Gonçalves et al. 2014).

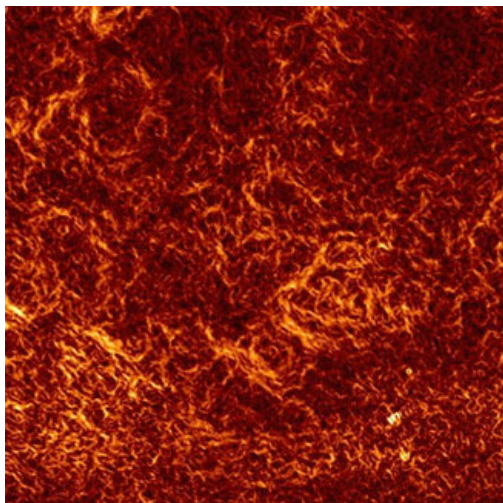
Liquids and gasses generally have a laminar, parallel flow at lower speeds, and become turbulent, swirling and forming eddies, at higher speeds (see Figure 2a) (Ball 2014). The transition from laminar flow to turbulent flow depends on the viscosity and velocity of the liquid or gas, since viscosity “smoothes” the flow and turbulence agitates it (Ball 2014). In the 1880’s, O. Reynolds investigated this transition from laminar to turbulent flow using pipes with dyed liquids (see Figure 3) (McDonough 2007). He came up with the dimensionless Reynolds number, which characterizes when this transition to turbulence happens by



(a) Laminar fluid flow from a faucet changes to turbulent flow as it hits a cup. In an astrophysical sense, this is analogous to a hot outflow from a star hitting colder ISM. Figure from Werne (2016)



(b) A hierarchy of eddies can be seen in the turbulent rapids in this river. Figure from Wayfarer (2016)



(c) A gradient image of linear polarization for a region of the Southern Galactic Plane Survey, illustrating interstellar turbulence. Figure from Gaensler et al. (2011).



(d) Bumpy rides from airplane turbulence is a commonly experienced form of turbulence. The eddies under this airplane are yet another. Figure from Morris/AirTeamImages (2007)

expressing the relative importance of inertial and viscous forces (Ball 2014).

$$Re = \frac{\rho U L}{\mu}$$

where ρ is the fluid density, μ the viscosity, U the velocity scale or a typical value of velocity or the average, and L a typical length scale like the radius of the pipe in Figure 3 (McDonough 2007).

The Reynolds number (Re) is the ratio of the flow speed to viscosity of the material (Ball 2014). A low Reynolds number ($Re \lesssim 2000$) implies that viscous forces are large and will result in laminar (smooth, constant, non-mixing) flow (McDonough 2007; Falceta-Gonçalves et al. 2014). A high Reynolds number ($Re \gtrsim 2300$) indicates viscous forces are small and inertial forces are large (McDonough 2007; Falceta-Gonçalves et al. 2014). Turbulence develops at high Reynolds numbers (McDonough 2007).

While the Reynolds number will tell you if a flow is turbulent, the Sonic Mach number is a way to quantify how much turbulence exists in a fluid.

The Sonic (M_s) Mach Number is defined as:

$$M_s = \frac{v}{c_s}$$

where v is the flow velocity and c_s the speed of sound in the medium (Vazquez-Semadeni 2012). The Sonic Mach number relates the flow velocity with the speed of sound in the fluid or gas.

Subsonic ($M_s < 1$) materials have a local sound speed/gas pressure greater than the flow velocity. They have less waves or perturbations and behave incompressibly (Vazquez-Semadeni 2012). This is what we tend to see everyday on Earth. Typical velocities of air

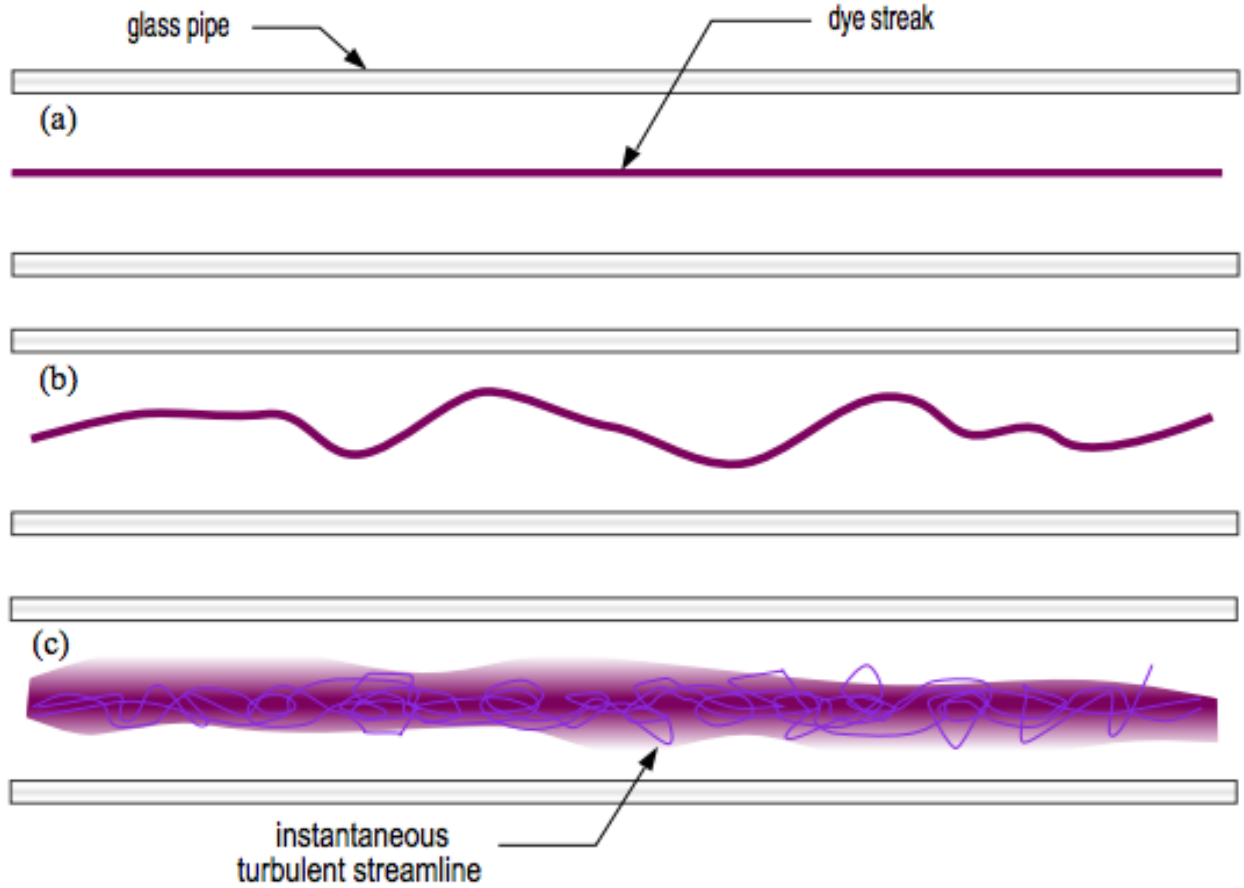


Fig. 3.—: The Reynolds experiment: (a) laminar flow corresponding to $Re \lesssim 2000$, (b) early transitional but still laminar/minimal mixing flow corresponding to $2000 \lesssim Re \lesssim 2300$, and (c) turbulence/significant mixing corresponding to $Re \gtrsim 2300$. Figure from McDonough (2007)

are much less than the speed of sound and gas densities on Earth are relatively unvaried; pressure forces in the atmosphere typically take care of overdensities that may develop before they have time to grow larger than the local sound speed.

Supersonic ($M_s > 1$) materials have a larger flow velocity than local sound speed, more turbulence, a range of gas densities, and behave compressibly (Vazquez-Semadeni 2012). This is what we tend to see in interstellar space, though turbulence, magnetic fields, and net cooling can change the compressibility of the gas (Vazquez-Semadeni 2012). Velocities of gas can be faster than the speed of sound and density can vary greatly in the ISM because strongly supersonic motions can cool gas rapidly and allow production of large amplitude density fluctuations (Vazquez-Semadeni 2012).

Though the Reynolds number and the Sonic Mach number help to characterize turbulent fluid flows, fluid flows can be described more completely by the Navier-Stokes equations. Both laminar and turbulent fluid flows of various Mach numbers follow the Navier-Stokes equations, which result from the application of Newton’s second law of motion to fluids (Ball 2014). The Navier-Stokes equations describe the physics of all fluid flows within the continuum hypothesis (McDonough 2007). The continuity or mass equation (1), momentum equation (2) and energy equation (3) for a compressible fluid (different equations exist for incompressible fluids) are:

$$\frac{\partial \rho}{\partial t} + \frac{\partial}{\partial x_j} [\rho u_j] = 0 \quad (1)$$

$$\frac{\partial}{\partial t} (\rho u_i) + \frac{\partial}{\partial x_j} [\rho u_i u_j + p \delta_{ij} - \tau_{ji}] = 0, \quad i = 1, 2, 3 \quad (2)$$

$$\frac{\partial}{\partial t} (\rho e_0) + \frac{\partial}{\partial x_j} [\rho u_j e_0 + u_j p + q_j - u_i \tau_{ij}] = 0 \quad (3)$$

Here, ρ is the density, p the pressure, t the time, u the flow velocity, τ the viscous stress, and q the heat-flux.

The Navier-Stokes equations map how energy, momentum, and mass are conserved in a fluid in terms of pressure, temperature, density, and velocity. However, they are non-linear and have non-local solutions (Falceta-Gonçalves et al. 2014). Solving these equations analytically is usually impractical (McDonough 2007). Instead, simplifying assumptions are made to analytically solve the equations, experimental data is gathered, or the full equations are studied numerically in computational fluid dynamics (McDonough 2007).

In 1941, Andrei Kolmogorov solved the Navier-Stokes equations for subsonic turbulent flow after assuming the energy transfer rate is constant at all scales and that the velocity scale follows a stochastic (random) distribution (Kolmogorov 1991; Falceta-Gonçalves et al. 2014). Subsequently, scaling laws, which describe statistical moments of velocity or velocity structure functions, could be used to model turbulence under these assumptions (Falceta-Gonçalves et al. 2014). Essentially, Kolmogorov calculated how much energy is contained in turbulent eddies of different sizes and showed that the energy and scale are related by a power law, $E(k) \propto k^{-5/3}$ (Ball 2014). Kolmogorov’s solutions were later transferred into Fourier space as a non-linear interaction between similar wavenumbers, creating a spectral form of the Navier-Stokes equations (Falceta-Gonçalves et al. 2014). This power spectrum shows one representation of the dependence of energy on wavenumber or frequency (see Figure 4) (McDonough 2007). Placing turbulence in the perspective of a spectrum of certain energies at certain scales, for which statistics could be calculated, removed it from a more physical interpretation (as eddies and vortices) but more easily illustrated scale relations in the energy cascade (Ball 2014). This theory of turbulence, often and hereafter referred to as K41, successfully reproduces most experimental data (Falceta-Gonçalves et al. 2014).

K41 works well for subsonic, turbulent flow, which is typical of fluids on Earth (McKee & Ostriker 2007). However, the ISM is supersonic, magnetized, and turbulent; magnetic fields influence the injection and evolution of turbulence and energy is dissipated through

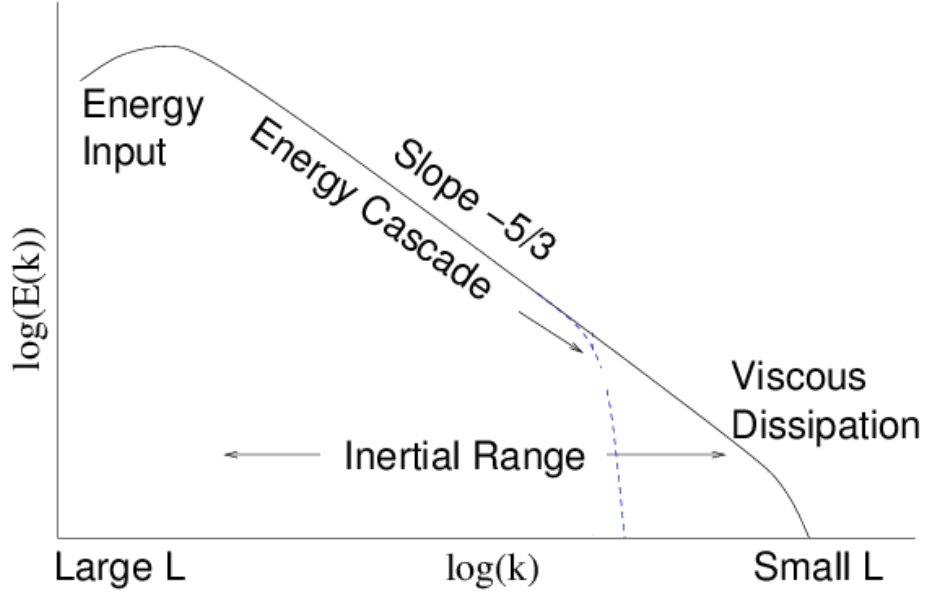


Fig. 4.—: An energy spectrum $E(k)$ of turbulence as a function of wave number, $k = 2\pi/L$. The inertial range, between the energy injection and viscous damping scales, is where the cascade follows a power law, $E(k) \propto k^{-5/3}$, as predicted by Kolmogorov (McDonough 2007; Falceta-Gonçalves et al. 2014). This range is where the energy transfer rate is constant (McDonough 2007; Falceta-Gonçalves et al. 2014). Eventually viscosity damps out the energy cascade. Figure from Hutchinson (2014).

not only the energy cascade but also shocks (Elmegreen & Scalo 2004; Lazarian 2004; McKee & Ostriker 2007). For the ISM, K41 is an approximation (Elmegreen & Scalo 2004; Lazarian 2004; McKee & Ostriker 2007). Though no complete and unified theory exists for supersonic, magnetized fluid flow (which characterizes molecular clouds), partial ones include Goldreich-Sridhar’s for subsonic magnetized turbulence and Fleck’s for supersonic flow (Falceta-Gonçalves et al. 2014). We later discuss Goldreich-Sridhar’s theory in the context of magnetohydrodynamic (MHD) turbulence in the ISM, and direct the reader to Fleck (1996) for more information on their theory.

1.3. Interstellar Magnetohydrodynamic Turbulence

Interstellar turbulence has different properties from typical turbulence on Earth; it is not statistically homogeneous, isotropic, or stationary (Elmegreen & Scalo 2004). Interstellar turbulence is further alienated from the more familiar, terrestrial turbulence by the incorporation of self-gravity, heating and cooling processes, and magnetic flux conservation (Vazquez-Semadeni 2012). One familiarity is that interstellar turbulence seems largely similar to classical incompressible turbulence, like that described by K41; energy appears to be injected on much larger scales (e.g. spiral density waves, shear instabilities, and superbubbles on a kilo-parsec scale) and then cascades down to smaller scales (e.g. supernovae, stellar winds, cosmic ray streaming on parsec to AU scales) (Elmegreen & Scalo 2004). Supernovae are thought to be the largest energy contributors, but other processes, like fluid instabilities, galaxy interactions, self-gravity, shock waves, and/or field star motions, can inject energy into the ISM (Elmegreen & Scalo 2004). In molecular clouds, the result of energy injection, the energy cascade, and subsequent turbulence is both a curb in global collapse due to a transferring of energy to fragments of smaller and smaller scales and also an encouragement of local collapse in cloud cores (Elmegreen & Scalo 2004).

Because the ISM is magnetized as well as fluid, the Navier-Stokes Equations are supplemented with Maxwell’s Equations to become MHD equations, assuming perfect coupling between magnetic fields and plasma (Falceta-Gonçalves et al. 2014). A magnetic Reynolds number exists, where the velocity is replaced with magnetic diffusivity. Reminiscent of the Sonic Mach number, the Alfvén Mach (M_a) number is used to describe the magnetic field strength:

$$M_a = \frac{v_L}{v_a}$$

where v_L the injection velocity and v_a the Alfvén velocity, ($v_a = B/\sqrt{4\pi\rho}$) (Vazquez-Semadeni 2012).

It is important to find whether magnetized regions in the ISM are sub-Alfvénic ($M_a < 1$) or super-Alfvénic ($M_a > 1$). Sub-Alfvénic mediums are shaped by their strong magnetic fields; the gas motions excited by turbulence are small compared to the mean magnetic field and so do not change the magnetic field configuration (Falceta-Gonçalves et al. 2008). Super-Alfvénic mediums are unrestricted by their weaker magnetic fields (Vazquez-Semadeni 2012). Their magnetic pressure is small compared to the kinetic energy of the turbulent gas so the mean magnetic field is easily distorted (Falceta-Gonçalves et al. 2008; Vazquez-Semadeni 2012). This creates large polarization dispersions and density fluctuations (Falceta-Gonçalves et al. 2008; Vazquez-Semadeni 2012). Turbulent fragmentation occurs in super-Alfvénic regions, producing strong shocks responsible for the density perturbations that condense molecular clouds and ignite star formation. Molecular clouds have MHD turbulence that is supersonic and super-Alfvénic (Falceta-Gonçalves et al. 2008; Vazquez-Semadeni 2012).

Measurements of small scale magnetic fields can be tedious and insensitive, so turbulence parameters like Alfvén Mach numbers are difficult to estimate (Burkhart 2014). Techniques like the VAT can be used instead. The presence of a magnetic field induces a preferred di-

rection for charged particle motion within the ISM, as discussed in Section 1.6 (McKee & Ostriker 2007; Burkhart et al. 2013). This causes the turbulent energy cascade to become anisotropic, meaning eddies are elongated along the direction of the magnetic field (see Figure 5) (Burkhart et al. 2013). Large scale motions in turbulent, magnetic ISM have more kinetic energy than small scale motions, resulting in similar values for the magnetic field at all scales (Burkhart et al. 2013). Consequently, the magnetic field influence does not dynamically prevail at large scales but does for small scales (Burkhart et al. 2013). This results in greater elongation as scales decrease (Burkhart et al. 2013).

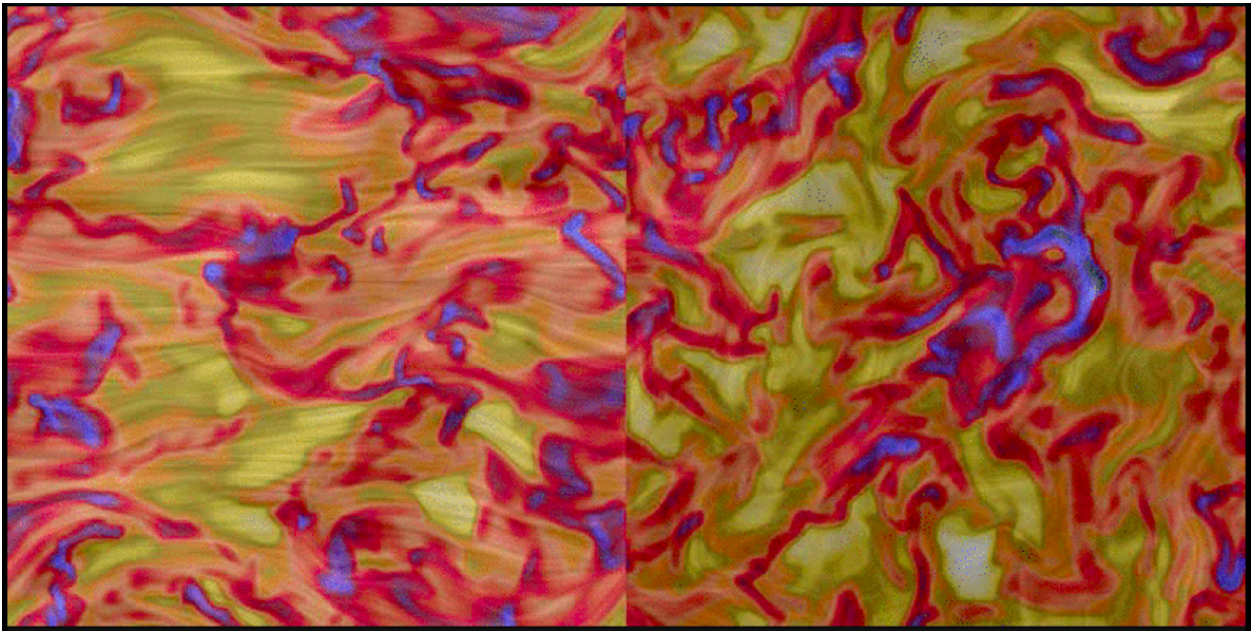


Fig. 5.—: Two perspectives of a numerical simulation of turbulence with a strong magnetic field. The image on the left has the magnetic field in the direction of the horizontal axis. Elongation of eddies are discernible when compared to the image on the right, whose magnetic field is directed inward, along our line of sight. The blue regions are higher density than the yellow by a factor of four. Simulation courtesy of Burkhart and Kowal et al. (2007).

While the Alfvénic Mach gives an estimate of magnetic field strength, a more thorough description of MHD turbulence would be helpful. The Goldreich & Sridhar (1995) theory

of incompressible magnetohydrodynamic (MHD) turbulence (hereafter GS95) is based on a critically-balanced anisotropic energy cascade. While K41 assumed the wave number and velocity of incoming perturbations were the same as those leaving via the energy cascade, GS95 does not. The energy cascade is the same in the perpendicular direction of the magnetic field as in K41, but is diminished in the direction parallel to the magnetic field (Goldreich & Sridhar 1995). Additionally, anisotropy increases on small scales (Goldreich & Sridhar 1995). This leaves detectable anisotropy both in the dispersion of eddy velocities and in the dispersion of wave numbers, though easier to observe anisotropic dispersion in velocity power spectra (Goldreich & Sridhar 1995). The balancing part of the critically balanced premise of GS95 theorizes that the timescale for energy to cascade along the two directions is comparable. If λ_{\parallel} and λ_{\perp} are the wavelengths parallel and perpendicular to the mean magnetic field and v_A and v are the Alfvénic and mean velocity fluctuations at those component scales, then the critical balance would look like (Goldreich & Sridhar 1995):

$$\lambda_{\parallel}/v_A \sim \lambda_{\perp}/v$$

An energy-conserving cascade has $v \propto \lambda_{\perp}^{1/3}$, so we find (Goldreich & Sridhar 1995):

$$\lambda_{\parallel} \propto \lambda_{\perp}^{2/3}$$

Thus, critically balanced Alfvénic cascade yields a scale dependent anisotropy of the λ_{\perp} velocity field (Goldreich & Sridhar 1995).

Because of GS95 MHD eddy elongation, astronomers can deduce Alfvénic Mach numbers from the anisotropy in the velocity field of the region (Burkhart 2014). Due to observation geometry, the actual anisotropy is always less than or equal to that which is observed along the line of sight; only a lower limit of anisotropy can be detected due to projection effects (Burkhart 2014). When our line of sight is perpendicular to the magnetic field, the estimated Alfvénic Mach number is an upper limit (Burkhart 2014). Dust polarization and Faraday

rotation measurements, further discussed in Section 1.4, could assist with complimentary plane of sky magnetic field estimations (Burkhart 2014).

1.4. Observing MHD Turbulence in the ISM

Strong observational indicators that the ISM is in fact turbulent are the ISM’s density distribution and velocity distribution (Dyson & Williams 1997; Burkhart et al. 2013; Falceta-Gonçalves et al. 2014). The velocity distribution is usually detected by non-thermal broadening of emission and absorption lines like HI and ^{12}CO and ^{13}CO (Dyson & Williams 1997; Burkhart et al. 2013; Falceta-Gonçalves et al. 2014). Statistics on the time and space variability of both the density and velocity fluctuations are used to study interstellar MHD turbulence, though velocity dispersions are favored (McKee & Ostriker 2007; Falceta-Gonçalves et al. 2014).

Low surface brightness of density tracers and projection effects complicates direct analysis of turbulent flows in the ISM (Falceta-Gonçalves et al. 2014). As a result, turbulence is typically studied with line of sight data (polarization, velocity dispersion from spectral lines, Faraday rotation) or in plane of the sky maps (integrated quantities like emission lines, column density, stokes parameters for polarization maps) (Falceta-Gonçalves et al. 2014). Column density projections/emission maps are also influenced by projection effects— that is, different structures projected on the same line of sight but decorrelated at a given length scale can be seen as a single structure in projected emission map (Falceta-Gonçalves et al. 2014). Other tracers of interstellar turbulence include the scintillation of background radiation/changes in refraction index due to turbulent motions in the ionized components of the ISM (yielding a density spectrum along line of site) and also the fluctuations of Faraday rotation measurements in the plane of sky if the magnetic field is known (Falceta-Gonçalves et al. 2014).

Techniques have been developed to extrapolate 3D turbulence information from available observations (spectral line data cubes from molecular transitions, continuum emission maps from dust, extinction maps from background stars, and polarization maps from dust) (McKee & Ostriker 2007; Lazarian 2011; Burkhart 2014). These include one point statistics (mass distribution, volume or density probability distribution functions), autocorrelation functions, power spectra, structure functions, fractal dimensions, multifractal spectra, hierarchical structure trees, clump mass functions, bispectrum, phase coherence, and principal component analysis (McKee & Ostriker 2007; Lazarian 2011; Burkhart 2014). Some of these techniques are further discussed in Section 1.7.

What do observations show us about MHD turbulence in the ISM? Turbulence in the ISM is mostly supersonic due to the large spatial scales in interstellar flows (Vazquez-Semadeni 2012). The amplitudes of velocity distributions for the ISM show there exists supersonic turbulent motion driven at scales from $\sim 10 - 100$ pc (Falceta-Gonçalves et al. 2014). On smaller scales, in different phases, and for different temperatures, the sound speed of the ISM varies, and subsequently the Sonic Mach number of turbulence in the ISM can vary (Vazquez-Semadeni 2012). For warm diffuse ionized regions in the ISM, turbulent flow is trans-sonic, $Ms \sim 1$, and gas behaves incompressibly (Ballesteros-Paredes et al. 2007; Vazquez-Semadeni 2012). Velocity fluctuations in this phase often cause density increases by pushing gas into thermally unstable regimes where it will then cool rapidly into colder, denser phases (Ballesteros-Paredes et al. 2007). In warm and hot ionized components of the ISM, turbulence is transsonic or subsonic and nearly incompressible (Vazquez-Semadeni 2012). Smaller scales are subsonic, with the exact scale depending on the ISM phase (Falceta-Gonçalves et al. 2014). Molecular clouds have subsonic turbulence at scales less than a parsec while warm and neutral diffuse phases are subsonic at a few parsec (because the local sound speeds are greater) (Falceta-Gonçalves et al. 2014). Observations show that the diffuse ISM is turbulent at scales > 150 pc and has a velocity dispersion of ≥ 50 km/s (Falceta-Gonçalves

et al. 2014). Modeling the ISM with first order energy injections of supernova driven outflows, galactic shear, and magneto-rotational instability and second order energy injections of local stellar feedback fit well to this data (Falceta-Gonçalves et al. 2014).

Line-width relations and power spectra illustrate the dominance of MHD turbulence in molecular clouds; MHD turbulence has been observed on scales of entire molecular clouds down to their cores (Ballesteros-Paredes et al. 2007; Burkhart et al. 2013). MHD turbulence not only governs molecular cloud formation and behavior but also affects the star formation processes; the elongation of eddies from MHD turbulence inhibits the collapse of molecular cores, decreases angular momentum, and builds filamentary structures which mediate the accretion rate of gas onto protostellar cores (Elmegreen & Scalo 2004; Ballesteros-Paredes et al. 2007). However, it does not inhibit global cloud collapse or align cloud fragments (Ballesteros-Paredes et al. 2007).

Supersonic and super-Alfvénic turbulence in dense molecular clouds generates further over-densities from which cores develop (Ballesteros-Paredes et al. 2007). These cores will eventually collapse to form stars. However, the process of star formation from the collapse of molecular clouds is inefficient; not all of the gas in molecular clouds ends up as stars (Vazquez-Semadeni 2012). The efficiency of molecular cloud mass to stellar mass conversion depends on both stellar feedback evaporating the surrounding molecular cloud material and the presence of magnetic fields (Ballesteros-Paredes et al. 2007). MHD turbulence contributes to low star formation efficiency by preventing large scale cloud collapse by transferring energy to fragments of smaller and smaller scales (Elmegreen & Scalo 2004; Ballesteros-Paredes et al. 2007; McKee & Ostriker 2007). However, MHD turbulence also encourages small scale collapse by small scale scattered ram-pressure compressions, which generate a greater range of gas densities, including densities that can collapse into stars and subsequently determining the lifetime of the cloud and its star formation rate (Ballesteros-Paredes et al. 2007; McKee

& Ostriker 2007; Vazquez-Semadeni 2012).

1.5. The Interstellar Magnetic Field

Our Galactic magnetic field is thought to be generated by a hydrodynamic dynamo (Ferrière 2001). Dynamo theory describes how motions of a conducting fluid embedded in a magnetic field can generate electric currents, which can amplify an original magnetic field. Our Galaxy’s dynamo process is its large scale differential rotation, complemented by small scale turbulent motions (Ferrière 2001). The Galactic dynamo still requires an original, “seed” magnetic field. This seed could have been an extragalactic magnetic field that existed before our Galaxy formed, a field that arose in protogalaxy formation, or fields from first generation stars which were spread into the ISM by winds and supernovae (Ferrière 2001).

Most of the galactic disk’s magnetic field has an intensity of $\sim 10 - 15 \mu\text{G}$ (Falceta-Gonçalves et al. 2014). In contrast, Earth has a field of $\sim 0.3 \text{ G}$, the Sun, $\sim 1 - 10^3 \text{ G}$, and pulsars $\sim 10^8 - 10^{13} \text{ G}$ (Ferrière 2001). HI regions have a magnetic field intensity of $2 - 10 \mu\text{G}$, and dense, molecular clouds have field intensities that increase with the square root of their density, somewhere on the order of μG to mG (Haverkorn 2014). Locally, the interstellar magnetic field is parallel to the galactic plane and the large scale magnetic field component is $\sim 6 \mu\text{G}$ (Ferrière 2001; Haverkorn 2014). Towards the center of our Galaxy, the field strength increases independently of ISM density, reaching $\sim 10 \mu\text{G}$ (Haverkorn 2014). Away from the center, the magnetic field follows the spiral arms of our Galaxy and is symmetric with respect to the Galactic plane (Haverkorn 2014). The magnetic field in Galactic halo is between $2 - 12 \mu\text{G}$ (Haverkorn 2014). Large scale reversals of magnetic field lines exist though their exact locations are debatable (Haverkorn 2014). Figure 7 shows a projected sky map of dust polarization, indicating magnetic field information for our Galaxy.

Traditionally, galactic magnetic fields are discussed as either small-scale and large-scale fields, though newer research includes a third, “random” component (Haverkorn 2014). Different names for these components are used in the literature, and are reproduced here for clarity. Large-scale/regular/uniform/coherent fields are coherent on length scales on the order of a galaxy and follow either the galaxy’s spiral arms or a ring shape (Haverkorn 2014). They are generated by galactic rotation and shear (a process that occurs when there is a velocity difference at the intersection of two fluids) (Falceta-Gonçalves et al. 2014; Haverkorn 2014). Small-scale/random/tangled/turbulent fields are associated with molecular clouds and star forming regions (Falceta-Gonçalves et al. 2014; Haverkorn 2014). They are generated by interstellar turbulence, supernovae, and remnants of shock waves, and are subject to the energy cascade (see Section 1.2) (Falceta-Gonçalves et al. 2014; Haverkorn 2014). Anisotropic random/ordered random/striated fields have a variable direction on small scales but a constant orientation on large scales (Haverkorn 2014). These fields stem from compression onto a 2D structure like in supernovae remnant shocks, spiral arm density waves, and/or galactic shears (Haverkorn 2014).

Magnetic fields affect their environment by inflicting a magnetic tension on embedded objects (Ferrière 2001). ISM clouds, for example, are threaded and connected by magnetic fields to intercloud medium and neighboring clouds (Ferrière 2001). The movement of any one cloud causes a deformity in the magnetic field lines and a tension/torque that restrains the cloud’s movement (Ferrière 2001). This restraint transfers the linear or angular momentum of a cloud to its environment (Ferrière 2001). This is a mechanism that is important for protostellar cores and star formation (Ferrière 2001). In HII regions, magnetic fields can exert a pressure on shells from bubbles and superbubbles, halting their expansion or collapse (Ferrière 2001). This results in thicker shells and quicker shell mergers (Ferrière 2001).

1.6. The Challenges of Observing Magnetic Fields

MHD turbulence plays fundamental roles in the ISM, star formation, and galaxy evolution. Studying it requires knowledge of interstellar magnetic fields. Dust polarization is considered the first solid evidence that the ISM is permeated by coherent magnetic fields (Ferrière 2001). The magnetic field in the ISM can be observed through techniques involving dust polarization, Faraday rotation, synchrotron emission polarization, Zeeman Splitting, the Goldreich-Kylafis effect, and the Chandrasekhar-Fermi method (Falceta-Gonçalves et al. 2014; Haverkorn 2014). Very occasionally, maser emission exists and these bright sources can also be used (Falceta-Gonçalves et al. 2014).

Many of the techniques for observing interstellar magnetic fields involves polarization, a fundamental property of electromagnetic radiation. Polarized light is detected when either the internal geometry of a radiation source or its local surroundings cause the light to prefer a particular orientation for its electric field vectors. Generally, interstellar radiation is elliptically polarized (its electric field vectors trace out an ellipse while propagating) (Trippe 2014). Light can also be linearly polarized and circularly polarized. In astronomy, the polarization state of a wave is most often described by its Stokes parameters, or characteristic intensities (Trippe 2014).

The starlight astronomers observe is usually linearly polarized by a few percent and proportional to the amount of extinction observed (Dyson & Williams 1997). Linear polarization occurs if dust grains are elongated (are cylindrically or elliptically shaped) and are oriented along a preferred direction (probably by magnetic fields) (Ferrière 2001; Dyson & Williams 1997; Trippe 2014). The dust then absorbs radiation as a function of the radiation’s orientation to the magnetic field, leaving behind linearly polarized light (Trippe 2014). Figure 6 illustrates a simple model of linear polarization, and Figure 7 displays polarization data from the Milky Way.

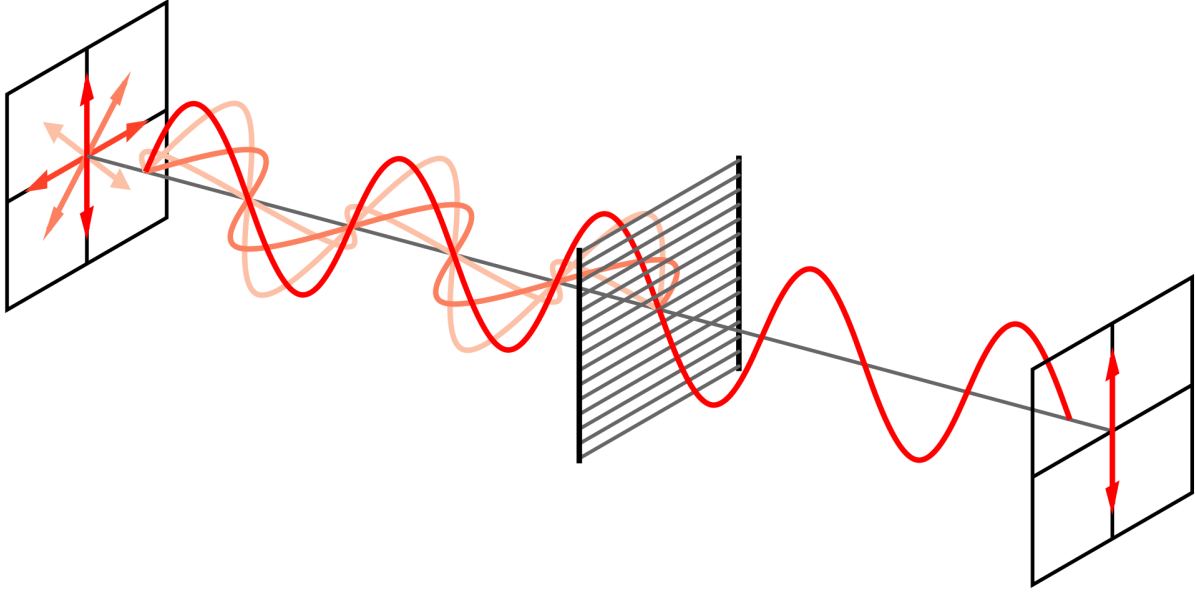


Fig. 6.—: A visual representation of linear polarization. The polarization of background stellar light can be caused by interstellar dust aligning similarly to the wire frame displayed on this image (Wikimedia Commons 2006).

The observation of the polarization of dust thermal emission is either in the far infrared and its absorption is in the visible and near infrared (Falceta-Gonçalves et al. 2014). Long axis aligned dust grains are perpendicular to the magnetic field and induce polarization parallel to the magnetic field (Falceta-Gonçalves et al. 2008). The mean polarization angle detected indicates the orientation of a large scale magnetic field (Falceta-Gonçalves et al. 2008). In addition, the polarization dispersion about the mean gives a value of the turbulent energy of the field, as further discussed in Section 1.2 (Falceta-Gonçalves et al. 2008).

Another line of sight magnetic field indicator is Faraday rotation. Faraday rotation occurs when waves propagate through a plasma within a magnetic field (Rybicki & Lightman 2007; Trippe 2014). In a magnetic field, plasma becomes dichrotic (absorbing radiation anisotropically, or more in one component than another) with respect to circular polarization

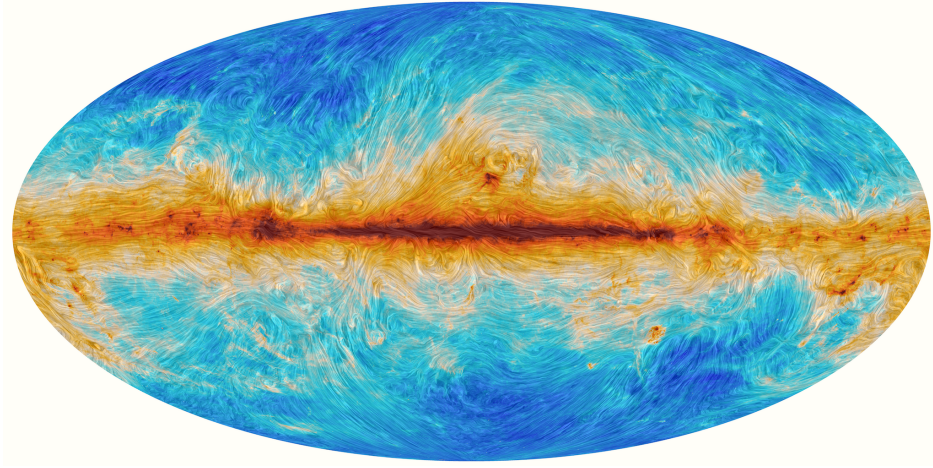


Fig. 7.—: ESA’s Planck satellite observed polarization from cosmic dust during its mission to map the cosmic microwave background radiation. Polarization emission can be used as a stand-in to trace the Galaxy’s magnetic field. In this image, color pertains to emission intensity and texture the magnetic field direction, which is perpendicular to the polarization direction (ESA & the Planck Collaboration 2015).

(Rybicki & Lightman 2007; Trippe 2014). Thus, the properties of waves depend on the direction of propagation as related to the direction of the magnetic field (Rybicki & Lightman 2007; Trippe 2014). Because of this discrimination between different polarizations, different polarizations will travel at different velocities in magnetized plasmas (Rybicki & Lightman 2007). A plane polarized wave, or a linear superposition of right-hand and left-hand polarized waves, will not keep a constant plane of polarization but rather one that rotates as it propagates, since either the right or left-hand polarization will travel at a greater velocity and receive a net phase shift (see Figure 8) (Rybicki & Lightman 2007).

Sources of linear polarization for Faraday rotation measurements are often pulsars or extragalactic radio continuum sources (Ferrière 2001). Pulsar observations are particularly helpful. Knowing the distance to a pulsar and calculating the rotation measure divided by the emission dispersion yields a weighted average of the strength of the magnetic field along

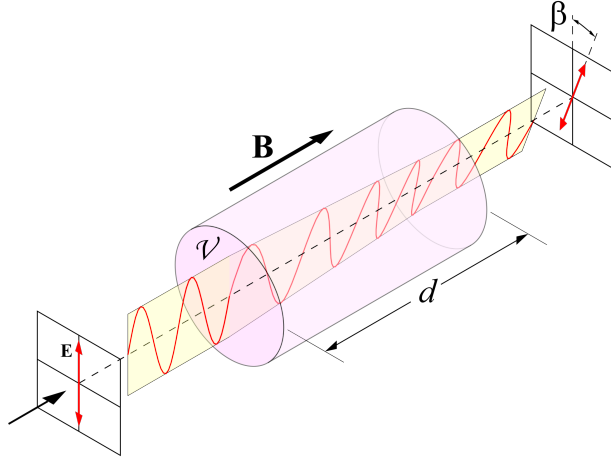


Fig. 8.—: Visualization of Faraday rotation, showing the net change in polarization angle (β) after the light has passed through a plasma with a magnetic field. Figure from Wikimedia Commons (2007).

the line of sight (Ferrière 2001).

Drawbacks of Faraday rotation measurements include its limitation to warm ionized medium (which has the most free electrons) and line of sight magnetic field components (Ferrière 2001). Synchrotron emission is often preferred as an alternative (Ferrière 2001).

Interstellar magnetic fields act on charged particles in the ISM through the Lorentz force. In all of the ISM except for the densest and coldest clouds (cores of molecular clouds) the gas is ionized enough for the neutral gas components to remain coupled with the ionized gas (via ion-neutral collisions), effectively “frozen” into the magnetic field (Dyson & Williams 1997; Haverkorn 2014). This allows astronomers to use observations of charged particles as a tracer for magnetic fields.

Electrons, gyrating around magnetic field lines at relativistic velocities, emit synchrotron radiation in a narrow cone along the particle’s trajectory (see Figure 9) (Rybicki & Lightman 2007; Sutton 2011; Trippe 2014). Synchrotron emission is polarized in the plane perpendic-

ular to the magnetic field and is mapped in order to probe the geometry of field lines in the plane of the sky (Falceta-Gonçalves et al. 2014). Both Faraday rotation and synchrotron emission probe the diffuse ionized medium to measure large scale magnetic fields but are not useful for denser and neutral phases of the ISM (Falceta-Gonçalves et al. 2014).

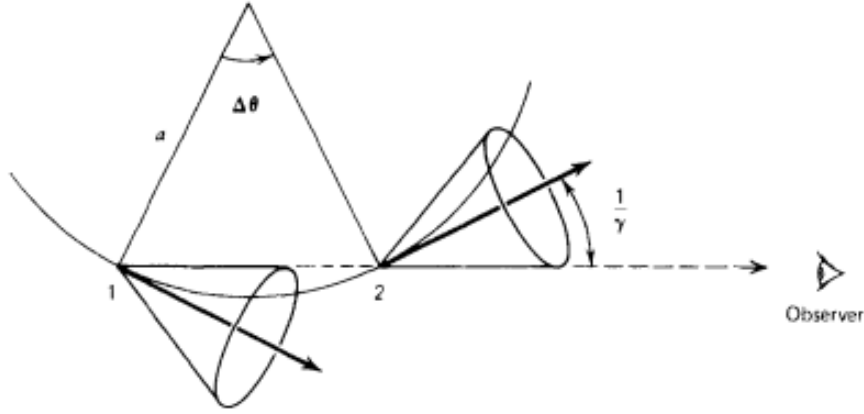


Fig. 9.—: Visualization of synchrotron radiation. If the magnetic field is in the x direction, towards the observer in this figure, the magnetic Lorentz force causes a circular motion of electrons in the y-z plane (Trippe 2014). A traveling electron in the x direction will then have a helical trajectory. For a stationary observer, the radiation will look like it is in a forward facing cone shape. When projected against the plane of the sky, the radiation looks elliptically polarized. Figure from (Rybicki & Lightman 2007).

While the polarization of thermal emission from dust grains, Faraday rotation, and synchrotron radiation measure the direction of magnetic fields, Zeeman splitting, the Chandrasekhar and Fermi (1953) technique and the Goldreich-Kylafis effect measure magnetic field strength.

Zeeman splitting is the splitting of atomic or molecular emission/absorption lines due to the presence of an external magnetic field (Ferrière 2001; Sutton 2011; Trippe 2014). The magnetic field causes a splitting of previously degenerate (giving the same spectral lines)

energy levels, yielding disparate spectral lines (Ferrière 2001; Sutton 2011; Trippe 2014). If the line of sight of the observer is perpendicular to the magnetic field lines, the spectral lines will appear linearly polarized (Trippe 2014). If the line of sight is parallel to the magnetic field lines, then the spectral lines will appear as circularly polarized (Trippe 2014). The amplitude of the splitting is directly proportional to the magnetic field strength (Ferrière 2001). Though the Zeeman effect can be observed from radio to UV in both atoms and molecules, Zeeman-splitting measurements are biased towards regions with high HI column densities and narrow 21cm line widths (towards cold neutral clouds) (Ferrière 2001). The Zeeman effect is also observed in CN for these high density regions, and in neutral hydrogen and OH in lower density regions (Sutton 2011; Falceta-Gonçalves et al. 2014).

Using the Zeeman effect to measure magnetic field strength is helpful for investigating the dense and cold ISM (Falceta-Gonçalves et al. 2014). When combined with dust/stellar polarization maps, Zeeman measurements are also useful for developing a 3D map of magnetic fields in molecular clouds (Falceta-Gonçalves et al. 2014). However, the Zeeman effect cannot be applied for clouds where line emission is weak (Falceta-Gonçalves et al. 2008).

When the Zeeman effect is weak, the Goldreich-Kylafis (GK) effect can be useful for tracing magnetic fields (Trippe 2014). If the radiation field is anisotropic, certain emission and absorption lines are excited preferentially (Trippe 2014). The resulting linear polarization is either parallel or perpendicular to magnetic field lines (Trippe 2014). GK polarization also depends on the velocity of the emission line profile, so it additionally contains velocity information along the line of sight (Trippe 2014).

If the ISM of interest is turbulent (See Section 1.2), the Chandrasekhar and Fermi (1953) technique (CF method) can be used. The CF method estimates the strength of an interstellar magnetic field along the plane of the sky by comparing linear or synchrotron polarization data with the velocity field (McKee & Ostriker 2007; Falceta-Gonçalves et al. 2014). Linear

polarization from dust emission or synchrotron radiation in a magnetized and turbulent plasma is effected by the strength of turbulence and the magnetic field (Trippe 2014). The CF method works on the assumption that the magnetic and kinetic pressures in the field are large, causing gas motions to be coupled to or “frozen” in with the magnetic field lines such that perturbations of the gas result in perturbations of the magnetic field lines (Falceta-Gonçalves et al. 2014; Trippe 2014). Using the dispersion of polarization angles and gas velocity fluctuations in the plane of the sky, assuming the magnetic/polarization fluctuations are Alfvénic (are like Alfvén waves) and the RMS velocity is isotropic, the strength of the magnetic field can be predicted (Falceta-Gonçalves et al. 2008). For weak magnetic fields, turbulent gasses drag the field lines around as they churn, yielding a large rms dispersion in polarization angles (Trippe 2014). For strong magnetic fields, the field lines are undisturbed by turbulence, yielding small values of polarization dispersion (Trippe 2014).

Unfortunately, all of these magnetic field observations tend to detect either one component of the field, like strength or the direction parallel or perpendicular to the line of sight, and/or in one particular tracer: ionized gas, dense cold gas, dense dust, diffuse dust (Haverkorn 2014). Our vantage point in the Milky Way also makes it difficult to observe the galactic magnetic field— making a 3D picture from 2D tracers involves many assumptions about the field, such as thermal and cosmic ray electron distributions, and local interstellar objects are hard to model (Haverkorn 2014). In practice, these techniques are often time consuming, involve complex and difficult data reduction, and require a great amount of telescope time (Esquivel & Lazarian 2011). Often, the resulting observations are insensitive and the resolution inadequate for the smaller scale structure where turbulence is studied (Esquivel & Lazarian 2011).

Consequentially, astronomers seek to deduce the magnetic field of a region by examining the statistical properties of emission line data (Esquivel & Lazarian 2011). If such a

method, like the VAT, were robustly developed, it would cut time and expenses in exploring interstellar magnetic fields.

1.7. Turbulence Statistics as Alternatives

Statistical descriptors which reveal the fundamental anisotropies in the ISM, like the VAT, can be used to study interstellar MHD turbulence. The turbulence power spectrum, which quantifies how much energy resides in a given eddy scale and is easily relatable to theoretical predictions, is an ideal statistical measure to have (Burkhart 2014). Typically, Fourier power spectra, in the form of spatial and velocity power spectra are often the statistics used (Burkhart 2014; Falceta-Gonçalves et al. 2014).

The 2D spatial power spectrum, which characterizes energy distribution over spatial scales, is perhaps the most common tool for studying MHD turbulence in the ISM (Burkhart 2014). From it, we can deduce the energy injection scale, inertial range, and dissipation range of turbulence (Burkhart 2014). A spatial power spectrum is computed from the slope of the Fourier transform of the two point autocorrelation function applied to integrated column density maps, and this slope depends on the Sonic Mach number of the turbulence (Burkhart 2014).

Density is a less direct measure of turbulence compared to velocity, but it is readily available from observations of column densities (Burkhart 2014). The velocity power spectra is preferable, but it is not as easily created as the density power spectra. Spectroscopic imaging measures line intensity as a function of position on the sky and velocity along an axis (Heyer et al. 2008). However, the shape of a line profile is dependent on density, the projected velocity component, temperature, chemical abundance, line excitation, and opacity (Heyer et al. 2008). It is also integrated along the line of sight, complicating the analysis

with projection effects (Heyer et al. 2008).

Both of these density and velocity power spectra have drawbacks— they use only the amplitudes of their Fourier transforms and ignore phase information, and are insensitive to magnetic field influences, so other statistical tools are sought out (Burkhart et al. 2013; Burkhart 2014).

Many statistical tools have been used to study turbulence, and an active goal of turbulence simulations is to provide as many of these descriptors as possible for the particular ISM region modeled (Elmegreen & Scalo 2004; McKee & Ostriker 2007; Burkhart et al. 2013; Burkhart 2014). In this thesis, we focus on the VAT as our descriptive statistic. Alongside of and within the VAT, we use structure functions of the distribution of radial velocity, principal component analysis, Sonic and Alfvénic Mach numbers. Brief overviews of the VAT, its structure functions, and PCA, with which we compare our results for the Taurus Molecular Cloud, are provided in Sections 1.7.1 and 1.7.2.

1.7.1. Velocity Anisotropy Technique (VAT)

In turbulence, order exists as scale dependent spatial correlations (McKee & Ostriker 2007). The goal of statistics for MHD turbulence is to determine the anisotropy of the cloud or cell. The challenge is discovering useful ways of analyzing available turbulence data to constrain MHD turbulence model predictions (Heyer & Brunt 2007). Anisotropies, as either larger dispersions or more power condensed perpendicularly to the magnetic field, can be revealed by comparison of the two points (Esquivel & Lazarian 2011). Two point statistics like power spectra, correlation functions, or structure functions can distinguish between K41 turbulence and GS95 anisotropic turbulence by calculating the inertial range slopes (Esquivel & Lazarian 2011). We use velocity structure functions in the VAT.

Spectroscopic rotational CO line emissions are the primary measurements for turbulence in the ISM, and a velocity structure function is one way of determining the degree of spatial correlation of velocities in these data (Heyer & Brunt 2007). The velocity structure function is a statistical measure of the n^{th} order of velocity differences as a function of spatial displacement, or lag (Heyer & Brunt 2007). In the inertial turbulence range, the structure function should vary as a power law with spatial lag (Heyer & Brunt 2007). The power law index is a measure of this spatial correlation and is what different turbulence models make predictions of (K41 predicts an index of $1/3$, for example) (Heyer & Brunt 2007).

We define our two-dimensional structure function as

$$SF(\mathbf{r}) = \langle [f(\mathbf{x}) - f(\mathbf{x} + \mathbf{r})]^2 \rangle \quad (4)$$

and use it to compute velocity anisotropy. Here, \mathbf{x} is the location of the measurement and \mathbf{r} is the distance between measurements, or spatial lag.

Velocity anisotropy is the difference of either directional power spectra or structure functions along two orthogonal directions of the velocity field. The degree of velocity anisotropy aligned with the magnetic field detected in a turbulent material can be used to indirectly measure the influence of an interstellar magnetic field on the ISM (Burkhart 2014). Large degrees of velocity anisotropy will occur when the magnetic field is strong and the Alfvén Mach number less than one (Heyer & Brunt 2011).

If the turbulence were isotropic (like K41 turbulence), the structure function would only depend on the distance between any two points (Lazarian 2004). In this case, plotting the structure function of a velocity centroid would reveal circular contours (Lazarian 2004). Because MHD turbulence is anisotropic, these contours become elongated along the magnetic field axis, forming elliptical contours and revealing the presence of the magnetic field (see Figure 10) (Lazarian 2004).

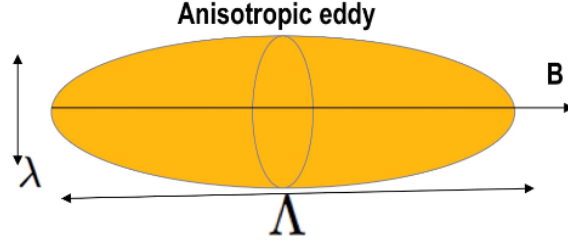


Fig. 10.—: A model of velocity anisotropy, showing an elongated eddy in the direction of the magnetic field. Here, Λ is the scale parallel and λ the scale perpendicular to the mean magnetic field. Figure from Blakesley Burkhart, CfA.

Commonly, velocity centroids, or the first moment maps, are used to obtain these velocity statistics when density fluctuations are minimal (Lazarian & Esquivel 2003). We create the velocity centroids by taking the product of intensity and velocity and then integrating over all velocities. Though velocity centroids are often used with two point statistics like structure functions to find velocity anisotropy, the effects of including radiative transfer on velocity anisotropy technique are unknown. Discovering these effects is another motivation of this thesis.

Constructing structure functions would be simple if we observed velocity fields rather than spectral line emission, which is a combination of line of sight density, velocity, temperature integration, and noise (Heyer & Brunt 2007). Position-Position-Velocity (PPV) data cubes are often reduced into a 2D image where each pixel is an estimate of the velocity centroid of the line emission (which are determined by fitting a line profile to the line emission) (Heyer & Brunt 2007). The statistics of velocity centroids can be related to that of 3D velocity fields, so velocity centroid images can be used to generate a power spectrum for which to apply a structure function meaningfully (Heyer & Brunt 2007).

1.7.2. *Principal Component Analysis (PCA)*

Principal component analysis, or PCA, is another technique for identifying anisotropy. PCA also seeks to recover the length scale dependence of turbulent velocity fluctuations, and is particularly advantageous for low signal-to-noise data (Brunt & Heyer 2013). It can obtain the velocity spectrum and Alfvénic Mach number for a region of MHD turbulence (Burkhart 2014).

PCA transforms data to a new set of variables, the principal components, which are linearly uncorrelated and ordered so that the first few retain most of the variation present in all of the original variables (Jolliffe 2002). All of the principal components are orthogonal eigenvectors of a covariance matrix, so PCA determines set of orthogonal axes along which data variance is maximized (Jolliffe 2002; Burkhart 2014). In this way, PCA reduces the dimension of a data set of many correlated variables to linearly uncorrelated ones while retaining as much of the variation in the data set as possible (Jolliffe 2002). For ellipsoids, the first principal component would be the major axis, because it would have the largest variance, and the second principal component would be the minor axis (Jolliffe 2002). For velocity data, the principal components would be the velocity channels (Burkhart 2014).

Drawbacks of PCA include its dependence on the scaling of the original data, its lack of orientation constraints which can dilute anisotropic data, and its reliance on an empirical calibration to translate the PCA power law index calculated from the velocity structure function or power spectrum to the true power law index in synthetic and real turbulence observations (Jolliffe 2002; Heyer et al. 2008; Brunt & Heyer 2013).

Using a structure function requires an averaging to create velocity centroids, but PCA is applied to data in Position-Position-Velocity (PPV) space. This has the advantage of avoiding loss of information from averaging. For a PPV velocity data cube, the spectrum/line profile of at each spatial grid point is the quantity subjected to the PCA (Brunt & Heyer

2013).

The PPV data cube is rearranged into sets of eigenvectors and eigenimages (Heyer & Brunt 2007; Heyer et al. 2008). The eigenvector is a velocity function that describes the velocity magnitude of line profile differences due to turbulence and other effects (Brunt & Heyer 2013). An eigenimage is a spatial function which indicates where in the sky these line profile differences occur (Brunt & Heyer 2013). The eigenimage is the integration of data over the velocity axis with the eigenvector acting as a weight (Brunt & Heyer 2013). The first two eigenimages are closely related to the 0th moment (integral of $T(v)$) and 1st moment (integral $T(v)v$), but with an additional velocity weight (Brunt & Heyer 2013). Together, eigenvectors and eigenimages are a principal component (Brunt & Heyer 2013).

If our data cube is represented as $T(\mathbf{r}_i, v_j) = T_{ij}$, where \mathbf{r}_i is the spatial coordinate of the i^{th} spectrum in the data cube, then the covariance matrix can be calculated as:

$$S_{jk} = S(v_j, v_k) = \frac{1}{n} \sum_{i=1}^n T_{ij} T_{ik}$$

where n is the number of spectra in the cube (Brunt & Heyer 2013). An eigenvalue equation for the covariance matrix,

$$S_{jk} u_{mj} = \lambda_m u_{mj}$$

can be solved for a set of eigenvectors, $u_{mj} = u_m(v_j)$, and eigenvalues, λ_m , which is the amount of variance projected onto its eigenvector (Brunt & Heyer 2013). Eigenimages, $\mathbf{I}_m(\mathbf{r}_i)$ can be constructed from projected values of the data cube onto the eigenvectors:

$$\mathbf{I}_m(\mathbf{r}_i) = \sum_{j=1}^p T_{ij} u_{mj}$$

where p is the number of spectroscopic channels per spectra in the data cube (Brunt & Heyer 2013).

The velocity differences and spatial scales are then derived for each principal component and linked to a velocity structure function through comparison with model velocity and density fields (Heyer & Brunt 2007; Heyer et al. 2008).

Heyer & Brunt (2011) uses PCA on the Taurus Molecular Cloud. We aim to compare the results of our velocity anisotropy technique with their PCA results on the same data.

2. The Scope of this Thesis

Developing and testing of techniques such as the VAT allows for more flexibility and potentially better accuracy when describing the ISM throughout our galaxy. Additionally, statistical testing provides cost and time advantages over direct observation of regions with magnetic fields and can use publicly available surveys. With this in mind, we investigate the results of the VAT for the first time on both CO radiative transfer simulations (Burkhart et al. 2014) and CO emission line data from the the Five College Radio Astronomy Observatory (FCRAO) Survey of the Taurus Molecular Cloud (Narayanan et al. 2008). By applying the VAT for the first time to CO radiative transfer MHD simulations, we can assess the effects of optical depth on measurements of the magnetic field strength. By applying the VAT to real molecular cloud data for the first time, we can test the feasibility of this statistic and develop practical methods for its application to real data.

First, we apply our structure function (see equation 4) to compressible MHD turbulence simulations with and without radiative transfer, to establish if there is a trend between velocity anisotropy and Sonic Mach number for various parameters of MHD turbulence. We begin with a discussion on the usefulness and computation of MHD turbulence simulations, in Section 3.1. Then we apply the VAT to emission line measurements in the Taurus Molecular Cloud. The data are described in Section 3.2. The methodology of the VAT for both

applications is described in Section 4 and the results are given in Section 5. We conclude by comparing our results with previous PCA anisotropy measurements on the same data from Heyer & Brunt (2011).

3. The Data

3.1. Simulating MHD Turbulence with Radiative Transfer

Observations of turbulent ISM regions are not the most helpful in understanding MHD turbulence; they yield only a snapshot of the effects of turbulence, are spatially limited, only include line of sight motions, and tend to be noisy (Esquivel & Lazarian 2011). In addition, the anisotropy information that is available through observational data is averaged along the line of sight, and is in reference to the mean magnetic fields of the field rather than the local magnetic field within the eddies, which is where the GS95 theory becomes important (Esquivel & Lazarian 2011; Burkhart 2014).

Numerical simulations are particularly helpful for modeling MHD turbulence because they can reproduce the structures and scaling laws we see in the ISM while showing us the values of underlying parameters (Burkhart 2014; Falceta-Gonçalves et al. 2014). These parameters include the Reynolds number, the Sonic and Alfvénic Mach number, energy injection scale, equation of state, and radiative transfer (Burkhart 2014). It is the comparison of turbulent MHD numerical simulations with different parameters to observations that helps researchers model MHD turbulence. Going one step further, the comparison of statistical test results to the parameters of these numerical simulations helps researchers design good statistical tests for MHD turbulence (Burkhart 2014).

Developing numerical simulations of interstellar turbulence is a way of observing turbulence in action. Though the simulations are simplified, they are beneficial in that they have

only user specified noise and spatial limitations and any existing anisotropies can be seen in reference to the local magnetic field (Esquivel & Lazarian 2011). As these simulations grow in sophistication, realistic cooling, ionization, chemistry, radiative transfer, ambipolar diffusion, magnetic reconnections, and realistic forcing can be incorporated, giving us an increasingly better model of MHD turbulence in the ISM. The simulations used in this thesis include the physical processes of thermal line broadening, cloud boundaries, noise, and radiative transfer effects.

The biggest drawback to numerical simulations is that current computational resources cannot generate a resolution that would yield Reynolds numbers like those observed in the ISM (Burkhart 2014). Nevertheless, the simulations can still be beneficial if the inertial range of the turbulence is resolved (see Figure 4) and the energy flux through the inertial range is constant (Burkhart 2014).

For this thesis, we use 3D MHD simulations of isothermal compressible turbulence generated from the Cho & Lazarian (2003) MHD code. We drive the turbulence with large-scale solenoidal forcing, and vary the input values for the sonic and Alfvénic Mach numbers (M_s and M_A). We include sub-Alfvénic ($B_0 = 1.0$), and super-Alfvénic ($B_0 = 0.1$) simulations, as well as the effects of thermal broadening.

The code is a second-order-accurate hybrid essentially nonoscillatory (ENO) scheme (Cho & Lazarian 2003). It solves the ideal MHD equations in a periodic box:

$$\frac{\partial \rho}{\partial t} + \nabla \cdot (\rho \mathbf{v}) = 0, \quad (5)$$

$$\frac{\partial \rho \mathbf{v}}{\partial t} + \nabla \cdot \left[\rho \mathbf{v} \mathbf{v} + \left(p + \frac{B^2}{8\pi} \right) \mathbf{I} - \frac{1}{4\pi} \mathbf{B} \mathbf{B} \right] = \mathbf{f}, \quad (6)$$

$$\frac{\partial \mathbf{B}}{\partial t} - \nabla \times (\mathbf{v} \times \mathbf{B}) = 0, \quad (7)$$

with the zero-divergence condition, $\nabla \cdot \mathbf{B} = 0$, and an isothermal equation of state $p = C_s^2 \rho$, where p is the gas pressure. The magnetic field, initially $\mathbf{b} = 0$, consists of the uniform

background field plus a fluctuating field: $\mathbf{B} = \mathbf{B}_{\text{ext}} + \mathbf{b}$.

The turbulence was driven solenoidally, at wave scale k equal to about 2.5 (2.5 times smaller than the size of the box), which defines the injection scale in our models in Fourier space and minimizes the influence of the forcing on the generation of density structures. In the equations above, the source term is \mathbf{f} , and is a random large-scale driving force ($\mathbf{f} = \rho d\mathbf{v}/dt$).

As the MHD waves in the simulation interact, density fluctuations are generated. The length, L , is in units of the energy injection scale. The time, t , is in units of the large eddy turnover time.

The models were grouped corresponding to sub-Alfvénic ($B_{\text{ext}} = 1.0$) and super-Alfvénic ($B_{\text{ext}} = 0.1$) turbulence. In each group, models were computed with different values of gas pressure, P (the control parameter that sets the sonic Mach number).

Resolutions of 512^3 and 256^3 , run time $t \sim 5$ crossing times so that the energy cascade is fully developed, and rms velocities close to unity ($v_{\text{rms}} \sim 0.7$) were used. Initial conditions include $\rho = 1$ and the Alfvén speed $v_a = |\mathbf{B}|/\sqrt{4\pi\rho}$.

Numerical modeling of MHD turbulence is done in 3D (Burkhart 2014). In order to compare the models with real observations, the 3D simulations are transformed into “synthetic” observations, by adding effects you would see when using a telescope, like noise, beam smoothing, radiative transfer, 2D projection effects, and etc. (Burkhart 2014). The output of this transformation can be a column density map, integrated intensity map, spectral line, or position-position-velocity (PPV) data cube (Burkhart 2014). The synthetic observations used in this thesis are PPV cubes, which we use to make synthetic velocity centroid maps. Parameters for these simulations are provided in Table 2.

After the PPV cubes were generated, the SimLine-3D radiative transfer algorithm (see

(Ossenkopf 2002)) was applied (Burkhart et al. 2013). This code computes the local excitation of molecules from collisions with the surrounding gas. It also computes the radiative excitation at the frequencies of the molecular transitions through line and continuum radiation from the environment (Burkhart et al. 2013). This code is an approximation, but it has an expected accuracy of better than 10 %, which is on par with observational calibration error (Burkhart et al. 2013).

For the SimLine-3D radiative transfer algorithm, the number density scaling factor (in units of cm^{-3} and denoted with the symbol n) and the molecular abundance (CO/H_2 , denoted with the symbol ab) were varied. This varied the optical depth, τ , generating both optically thin and thick models. Integrated intensity maps that show the variation caused by adjusting density and abundance values for these simulations and are given in Section 6.

For further details on these simulations see Burkhart et al. (2014); Cho & Lazarian (2003); Kowal et al. (2007); Burkhart et al. (2009); Esquivel & Lazarian (2011). Some simulations used were previously developed as a part of Burkhart et al. (2014).

3.2. Taurus Molecular Cloud Emission Data

Turbulence plays an important, though not well described role in the formation and evolution of molecular clouds. Molecular clouds are present in the spiral arms of the Milky Way and are the first indications of gravitational instabilities in our Galaxy (Ballesteros-Paredes et al. 2007). These instabilities drive spiral density waves, or density perturbation which move along at different velocities than those of the objects within it, and causes local gravitational collapse (Ballesteros-Paredes et al. 2007). These density waves are also what gives the Milky Way and other galaxies their spiral arms (Ballesteros-Paredes et al. 2007).

We observe molecular clouds by interpreting optical absorption lines, UV spectra, and

Model	B_0	$\langle P_{\text{gas},0} \rangle$	M_s	M_A	Resolution
L2	0.1	0.01	~ 5.7	~ 5.7	512^3
L5	0.1	0.1	~ 1.8	~ 5.8	512^3
L6	0.1	1.0	~ 0.6	~ 5.8	512^3
L10	1.0	0.01	~ 5.5	~ 0.5	512^3
L13	1.0	0.1	~ 1.8	~ 0.6	512^3
L14	1.0	1.0	~ 0.6	~ 0.6	512^3

Table 2:: MHD Simulation Parameters. This table is recreated in part from Burkhart et al. 2014 where those simulations have been included. $\langle P_{\text{gas},0} \rangle$ and B_0 correspond to the initial gas pressure and magnetic field. Units for these quantities are dimensionless code units. They can be converted with the use of appendix A of Hill et al. (2008). The simulations used in this thesis were converted to physical units after the application of the SimLine-3D radiative transfer algorithm.

radio waves. The most abundant interstellar molecule is H_2 , which is observable from UV spectra (Ferrière 2001). Unfortunately, UV spectra cannot be obtained for the interior of dense molecular clouds due to dust extinction (Ferrière 2001). As an alternative, radio waves, which have longer wavelengths and so are unaffected by dust, can be used to study molecular clouds. Since H_2 is diatomic, it is not observable in radio. CO, which has a $J = 1 \rightarrow 0$ rotational transition at a radio wavelength of 2.6 mm is often used instead to trace molecular gas (Ferrière 2001).

By using CO as a tracer for molecular clouds, astronomers have deduced that most molecular gas in the Milky Way is in a ring from 3.5 kpc to 7 kpc from the Galactic center and in a disk interior to 0.4 kpc (Ferrière 2001). Most of the remaining molecular gas is in the spiral arms (Ferrière 2001). Figure 11 illustrates the observed molecular cloud placements in the Milky Way.

The Taurus Molecular Cloud is a well observed molecular cloud, primarily due to its position. It is ~ 140 pc away and displaced from the Galactic plane by about -19 degrees (Narayanan et al. 2008). This displacement allows for higher spatial resolution with little confusion with background objects, unlike most molecular clouds we see in Figure 11 (Narayanan et al. 2008).

Previous observations have shown the Taurus Molecular Cloud to have significant velocity dispersion anisotropy, indicating a GS95 type turbulence (Heyer & Brunt 2011; Falceta-Gonçalves et al. 2014). It has been found that the densest regions of the cloud have super-Alfvénic turbulence and the less dense surrounding materials have sub-Alfvénic turbulence (Heyer & Brunt 2011).

The data are wide field spectroscopic imaging of ^{12}CO and ^{13}CO $J = 1 - 0$ emission from the Five College Radio Astronomy Observatory (FCRAO) Survey of the Taurus Molecular Cloud described by Narayanan et al. (2008). The survey imaged 96 square degrees of the

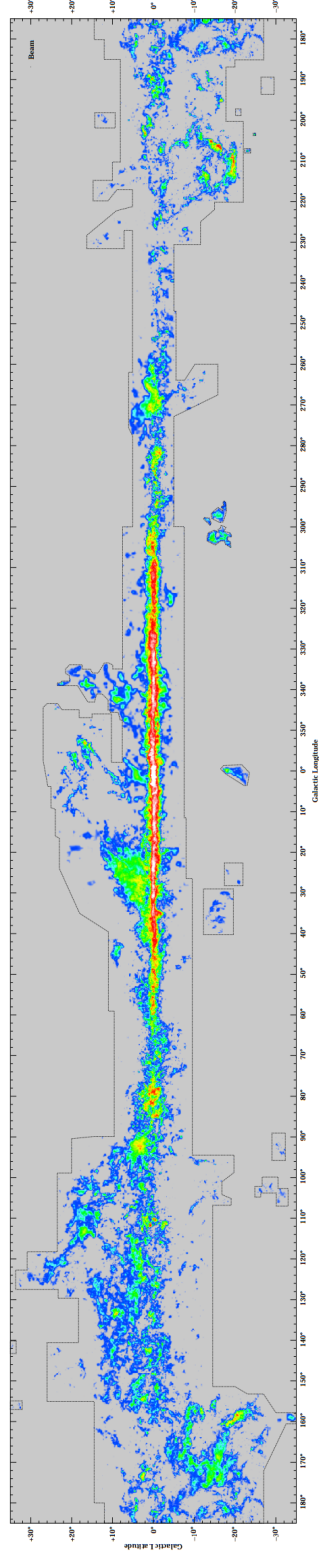


Fig. 11.—: A velocity-integrated map of CO, which traces out the distribution of molecular clouds in our Galaxy (Dame et al. 2001). Redder colors mark higher gas density.

Taurus cloud with 45'' (0.02 pc) resolution on the FCRAO 14 meter telescope Narayanan et al. (2008). The data were collected over two observing seasons (Nov. 2003 - May 2005) and the ^{12}CO and ^{13}CO line emission were observed simultaneously Narayanan et al. (2008).

The FCRAO 14 meter telescope front-end had a 32 element focal plane array receiver, SEQUOIA, that fed a set of 64 autocorrelation back-end spectrometers configured with a spectral resolution of 25 MHz and 1024 channels for both observed line transitions (Narayanan et al. 2008). The FWHM beam sizes of the telescope at the observed frequencies are 45'' (115.27 GHz) and 47'' (110.201GHz), the beam efficiencies 0.45 and 0.5 (calibrated to Jupiter), and spectral resolution of 0.076 km/s and 0.080 km/s, respectively (Narayanan et al. 2008).

The 98 square degree map was divided into 256 submaps, 30'x30' in size, and observed using an On-The-Fly (OTF) mapping technique (Narayanan et al. 2008). The data were deconvolved to account for contributions of antenna beam error and the line spectra resampled on the same spectral grid with 0.1 km/s spacing, due to the OTF technique generating irregularly sampled data (Narayanan et al. 2008). The data were outputted in 88 cubes without overlapping regions and with estimated calibration uncertainties of 0.87 km/s and 0.43 km/s for ^{12}CO and ^{13}CO , respectively (Narayanan et al. 2008).

The ^{12}CO line emission traces a diffuse molecular envelope, has low surface brightness, low visual extinction, and low gas volume density while the ^{13}CO line emission is relatively optically thin and associated with dense filaments (Narayanan et al. 2008). Heyer & Brunt (2011) found little velocity anisotropy in the ^{13}CO emission data set but did find anisotropy with super Alfvénic motions for ^{12}CO emission. This variation of anisotropy may be due to ionization changes from the diffuse envelope to denser filaments and core regions, or it may indicate the transition of MHD flow and illuminate the evolution of the cloud and the role of the magnetic field within it (Heyer & Brunt 2011).

We apply the same processes to the Taurus molecular cloud ^{12}CO and ^{13}CO $J = 1 - 0$ emission maps presented by Heyer & Brunt (2011). We compare our results with previously observed optical polarization.

4. Method of Applying VAT

For our synthetic observations, we began by calculating the PPV cubes with the intensity distribution

$$I(\mathbf{X}) \equiv \int \rho_s dV_{LOS}$$

where ρ_s is the intensity values or density of emitters of the 3D PPV data cube, \mathbf{X} the position on the plane of the sky, and V_{LOS} the line of sight velocity-axis. We integrate in velocity for the entire line of sight.

We next calculated the velocity centroid maps as the ideal centroid/first moment from the synthetic and observed PPV cubes as:

$$C_z(x, y) \equiv \frac{\int \rho(x, y, z) V_z(x, y, z) dz}{\int \rho(x, y, z) dz} \quad (8)$$

We applied our two-dimensional structure function (Equation 4) to the velocity centroid maps in Fourier space.

We then fit an ellipse to the outermost closed contour of each structure function map ¹.

The contour levels were generated arbitrarily, as they were only used to determine the angle of the major and minor axes. Taking the major and minor axes of this ellipse, we

¹An interactive python code for this analysis is hosted at https://github.com/mmcintosh27/velocity_anisotropy/blob/master/Structure%20Function.ipynb

calculated an anisotropy index as the average ratio of the structure functions in these two perpendicular directions to the line of sight (See Figure 12). For our simulations, this is the average ratio of eddy elongation along the horizontal and vertical axes:

$$SF_{C,z}(x, 0)/SF_{C,z}(0, y) \quad (9)$$

For the Taurus data (which was broken up into regions, see Figure 14a), the major and minor axes did not always line up with the vertical and horizontal axes (See Appendix), so a key function of the code was to calculate the offset angle of the axes with the horizontal. With the angle known, the correct axes could be selected to compute the average ratio of eddy elongation, yielding the average anisotropy index.

The anisotropy index lets us quantify an anisotropy increase with increasing magnetic field. For an isotropic contour (which would be generated by K41 turbulence), the anisotropy index would be one. For an infinitely anisotropic contour (a line), the anisotropy index would be zero. We compare the anisotropy index with the Sonic Mach number (See Figure 13), for all of our simulations. We compare our anisotropy index for the Taurus Molecular Cloud regions with the anisotropy reported by Heyer & Brunt (2011).

5. Results

First, we applied our structure function to compressible MHD turbulence simulations to establish if there is a trend between velocity anisotropy and Sonic Mach number for various parameters of MHD turbulence. Our results are displayed in Figure 13.

We see that for the optically thick case ($\tau > 1$) that the different magnetic field regimes are discernible and the velocity anisotropy generally increases with the Sonic Mach number. We see that for the optically thin case ($\tau < 1$) the nonradiative transfer simulations have a distinguishable regime per magnetic field value, but the radiative transfer simulations do

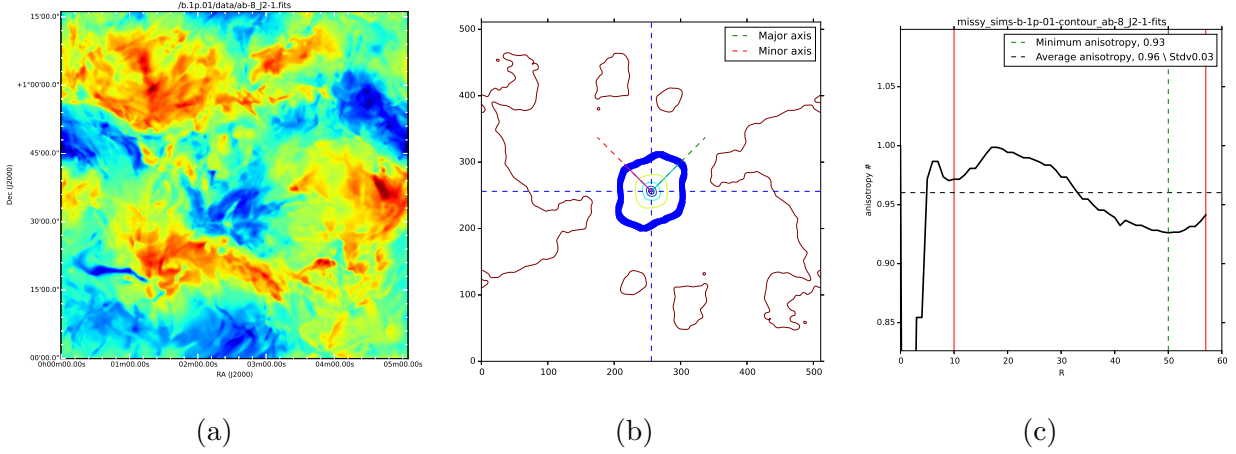


Fig. 12.—: One of the synthetic moment maps ($B = 0.1$, $P = 0.01$, and $ab=8$, for magnetic field, pressure, and abundance, respectively) (a) used with its accompanying structure function contour plot (b) and anisotropy index versus scale (c). The contour for which our measurement of the anisotropies extended to is highlighted in blue in figure (b). The average of the anisotropy was taken from the range in between the solid red lines in figure (c).

not.

This indicates that VAT may be most helpful for optically thick cases of MHD turbulence in the ISM. For molecular clouds, this means that ^{12}CO emission may be a better tracer for the VAT than the optically thinner ^{13}CO emission. To begin to quantify this relation, further simulations for which to apply the VAT could be produced with a greater range of optical thickness levels.

The anisotropy for nine regions in the emission data for the Taurus Molecular Cloud were calculated and are displayed in Figure 14a. These regions in Taurus proved to be mostly isotropic, with the lowest value of anisotropy being ~ 0.7 . This tells us that there is some variation in the magnetic field in the Taurus Molecular Cloud and that most regions are super-Alfvénic.

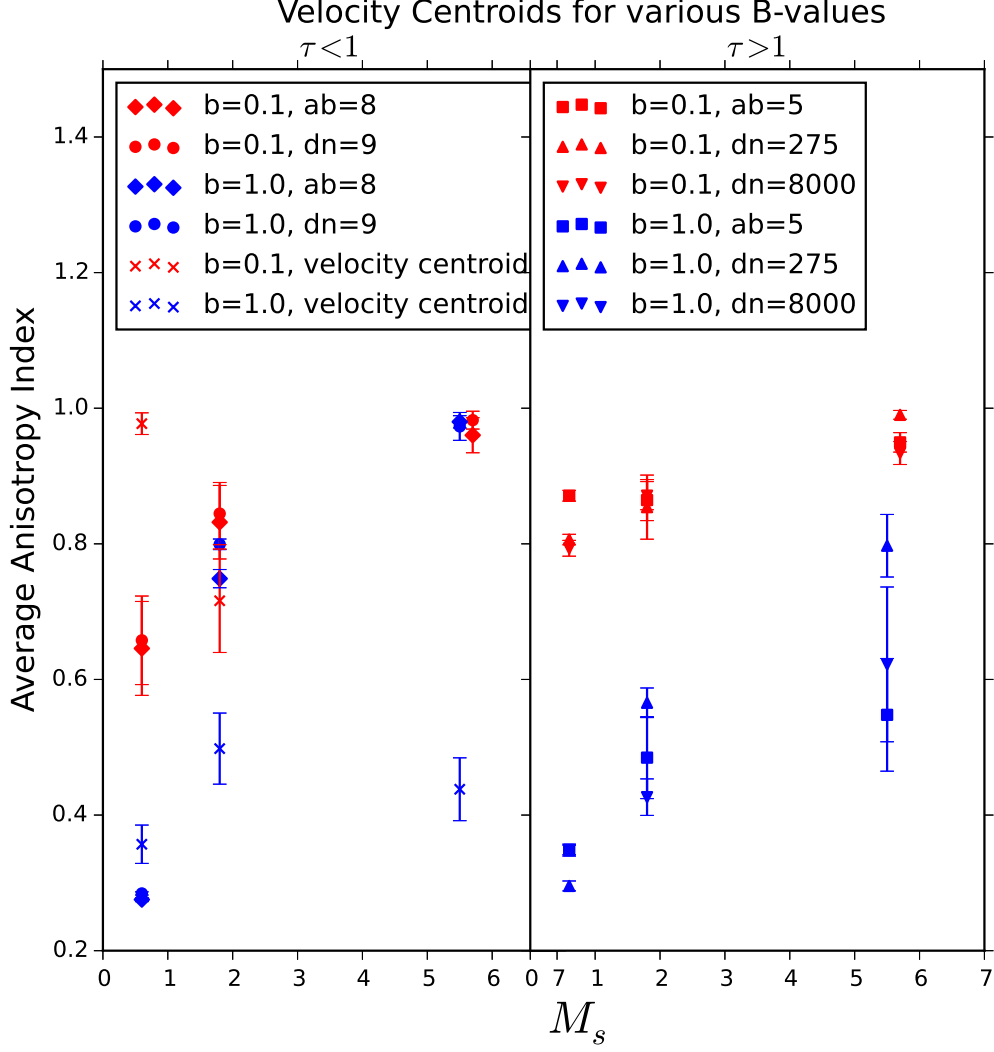
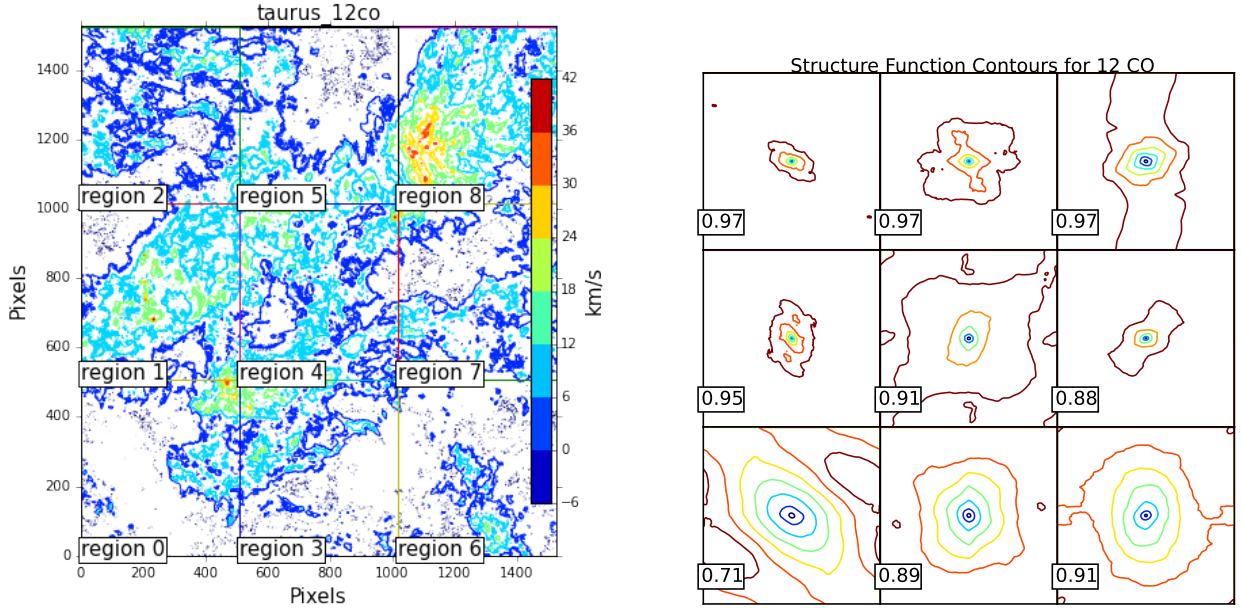
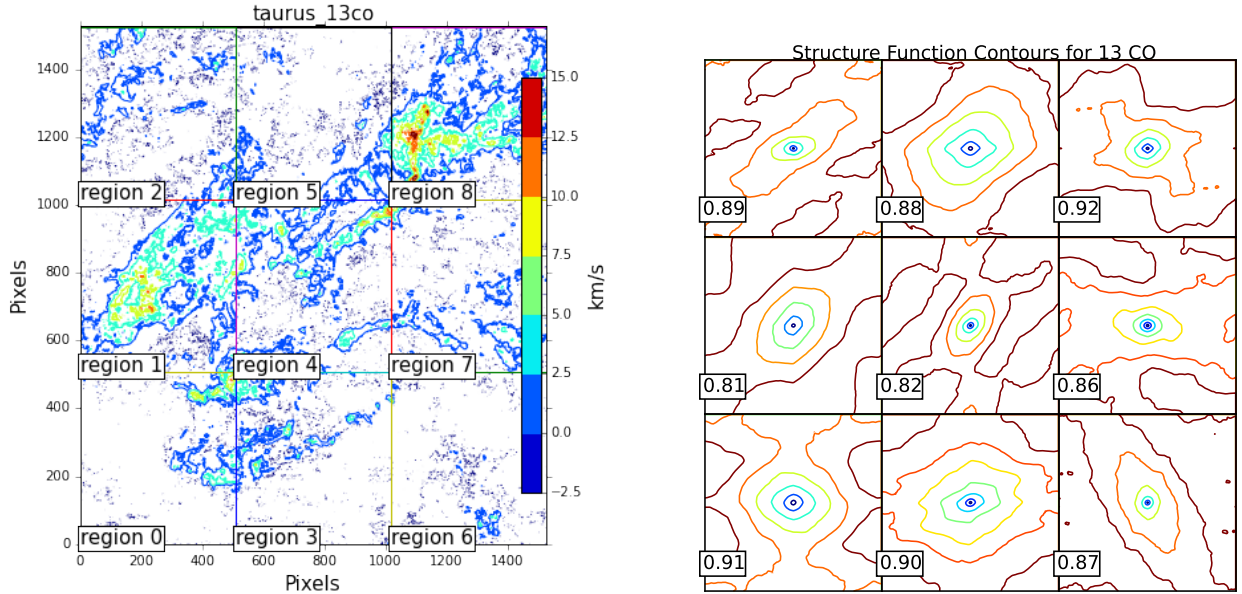


Fig. 13.—: The anisotropy index versus the Sonic Mach number for MHD radiative transfer simulations with various densities (“dn”) and abundances (“ab”) as well as nonradiative transfer simulations (“velocity centroid”) for different magnetic field strengths.



(a) First moment map for ^{12}CO emission of the Taurus Molecular Cloud and accompanying structure function contour plot. The listed anisotropy is the average, and the contour levels on the structure function plots are arbitrary.



(b) For ^{13}CO emission

Fig. 14.—: Moment Maps and Contour Plots for ^{12}CO and ^{13}CO Taurus Molecular Cloud

In their analysis of the Taurus Molecular Cloud emission data, Heyer & Brunt (2011) fit the phase and amplitude such that the degree of anisotropy was at a maximum. They did not account for projected substructure and so their anisotropy measurements are lower limits.

Heyer & Brunt (2011) found that in the Taurus Molecular Cloud, where surface brightness emission is low, the velocity anisotropy is largest. This corresponds to low gas column density or visual extinction areas. Our results did not reproduce this, though we used larger regions than Heyer & Brunt (2011). Using similar regions may show that the VAT follows anisotropy similarly to PCA, which would provide a check for the technique. However, Heyer & Brunt (2011) found that the north-east sector of the image has the strongest velocity anisotropy amplitudes, which is replicated in our results. We also found, like Heyer & Brunt (2011), that ^{12}CO emission showed more velocity anisotropy than ^{13}CO emission.

Further analysis for VAT results in the Taurus Molecular Cloud could include a comparison with known polarization data (see Figure 15) and an estimate of the Alfvénic Mach number of the regions.

6. Conclusion

In this thesis we presented a novel technique for measuring interstellar magnetic fields using velocity anisotropy. This technique is motivated by the cost and difficulty of obtaining direct magnetic field observations for studying MHD turbulence, a process that is fundamental to ISM dynamics, star formation, and the evolution of our Galaxy. We applied the VAT technique to radiative transfer MHD simulations and actual data for the first time.

We placed the importance of the VAT and studying MHD turbulence in the ISM in context by providing background on the ISM, its role in the Milky Way, its phases, structures,

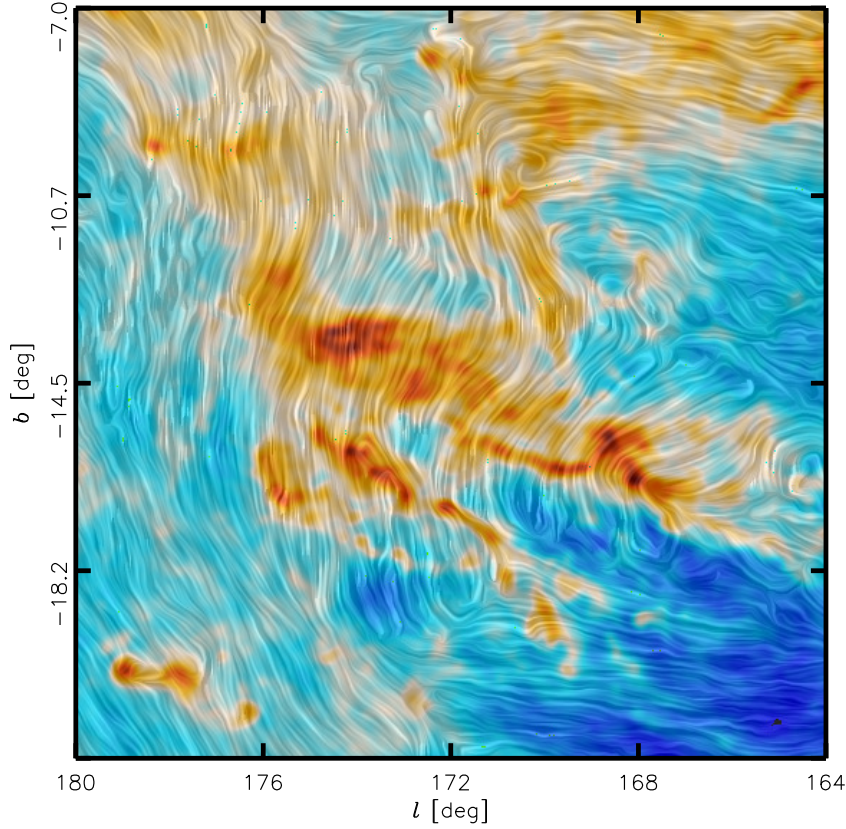


Fig. 15.—: Magnetic field and column density measured by Planck towards the Taurus Molecular Cloud. The colours represent column density and the The line pattern shows the orientation of magnetic field lines, orthogonal to the orientation of the dust polarization. Further analysis for VAT results in the Taurus Molecular Cloud could include a comparison with known polarization data such as this. Image and caption information from Planck Collaboration et al. (2016)

stellar interactions, molecular clouds, turbulent nature, and magnetic fields. We discussed turbulence theory, its resulting anisotropy which indirectly measures magnetic fields, and the challenges of producing direct magnetic field observations. We discussed the role of numerical simulations in studying MHD turbulence, the creation of synthetic observations, and various statistics for describing MHD turbulence with a focus on the VAT and PCA

technique.

We applied the VAT radiative transfer compressible MHD simulations and found that for the optically thick case ($\tau > 1$), the different magnetic field regimes are discernible and the degree of anisotropy generally increases with the Sonic Mach number. For the optically thin case ($\tau < 1$), the nonradiative transfer simulations have a distinguishable regime per magnetic field value, but the radiative transfer simulations do not. This has important implications for the sort of data (optically thick data, specifically) for which the VAT should be applied when using it to study MHD turbulence in the ISM. Further analysis steps with synthetic data could include generating simulations with a greater variation in optical depth parameters for which to apply the VAT. This could define more precisely what at optical depths the VAT traces turbulence effectively.

We then applied the VAT to ^{12}CO and ^{13}CO emission data from the Taurus Molecular Cloud. We developed an ellipse fitting routine to locate the structure function contour major and minor axes in observational data with which to compute the anisotropy index. This code was made public for future use.

In comparison to the PCA technique as presented by Heyer & Brunt (2011), we found our velocity anisotropy measurements did not also correspond to low gas column density or visual extinction areas, though this may be due to using larger regions for our structure function calculations. We did find that the north-east sector of the image has the strongest velocity anisotropy amplitudes, which is replicated in Heyer & Brunt (2011). We also found, like Heyer & Brunt (2011), that ^{12}CO emission showed more velocity anisotropy than ^{13}CO emission.

Further analysis steps for the Taurus Molecular Cloud data could include a comparison with known polarization data, using smaller regions, and calculating an estimate of the Alfvénic Mach number of the regions.

This study, and other future studies of MHD turbulence statistics allow us to derive magnetic field information from emission line observations, rather than more costly and time intensive direct magnetic field observations. Studying MHD turbulence in the ISM extends our knowledge of MHD turbulence, its effects on star formation, and its subsequent influence on the evolution of our Galaxy, underscoring the importance of developing techniques like the VAT.

REFERENCES

- Ball, P. 2014, The Scientific Problem That Must Be Experienced - Turbulence - Nautilus
- Ballesteros-Paredes, J., Klessen, R. S., Mac Low, M.-M., & Vázquez-Semadeni, E. 2007, *Protostars and Planets V*, 40, 63
- Brunt, C. M., & Heyer, M. H. 2013, *MNRAS*, 433, 117
- Burkhart, B., Falceta-Gonçalves, D., Kowal, G., & Lazarian, A. 2009, *The Astrophysical Journal*, 693, 250
- Burkhart, B., Lazarian, A., Leão, I. C., de Medeiros, J. R., & Esquivel, A. 2014, *The Astrophysical Journal*, 790, 130
- Burkhart, B., Ossenkopf, V., Lazarian, A., & Stutzki, J. 2013, *The Astrophysical Journal*, 771, 122
- Burkhart, B., Ossenkopf, V., Lazarian, A., & Stutzki, J. 2013, *ApJ*, 771, 122
- Burkhart, B. K. 2014, PhD thesis, The University of Wisconsin - Madison
- Cho, J., & Lazarian, A. 2003, *Monthly Notices of the Royal Astronomical Society*, 345, 325
- Dame, T. M., Hartmann, D., & Thaddeus, P. 2001, *ApJ*, 547, 792
- Dyson & Williams. 1997, in *The Physics of the Interstellar Medium*, Second Edition, 2nd edn., Series in Astronomy and Astrophysics (Taylor & Francis)
- Elmegreen, B. G., & Scalo, J. 2004, *Annual Review of Astronomy and Astrophysics*, 42, 211
- ESA, & the Planck Collaboration. 2015, *Polarised emission from Milky Way dust*
- Esquivel, A., & Lazarian, A. 2011, *The Astrophysical Journal*, 740, 117

- Falceta-Gonçalves, D., Kowal, G., Falgarone, E., & Chian, A. C. L. 2014, *Nonlinear Processes in Geophysics*, 21, 587
- Falceta-Gonçalves, D., Lazarian, A., & Kowal, G. 2008, *ApJ*, 679, 537
- Ferrière, K. M. 2001, *Reviews of Modern Physics*, 73, 1031
- Fleck, Jr., R. C. 1996, *ApJ*, 458, 739
- Gaensler, B. M., Haverkorn, M., Burkhart, B., et al. 2011, *Nature*, 478, 214
- Goldreich, P., & Sridhar, S. 1995, *ApJ*, 438, 763
- Haverkorn, M. 2014, 22
- Heyer, M., & Brunt, C. 2011, *Mnras*, 000, 2070
- Heyer, M., Gong, H., Ostriker, E., & Brunt, C. 2008, *ApJ*, 680, 420
- Heyer, M. H., & Brunt, C. 2007, in *IAU Symposium, Vol. 237, Triggered Star Formation in a Turbulent ISM*, ed. B. G. Elmegreen & J. Palous, 9–16
- Hill, A. S., Benjamin, R. A., Kowal, G., et al. 2008, *ApJ*, 686, 363
- Hubble Image, NASA, E. J. H., & of Arizona State University, A. L. 2005, *The Crab Nebula*, from News Release Archive
- Hubble Telescope, t. A. T. 2013, *A Molecular Cloud*, from Article 'Astronomers Begin to Map Galaxy's Giant Gas Clouds Where Stars are Born' by Tamarra Kemsley
- Hutchinson, I. H. 2014, *Schematic energy spectrum $E(k)$ of turbulence as a function of wave number $k=2/L$* , edited by me, from *Essential Numerical Methods*
- Jolliffe, I. 2002, *Principal Component Analysis* (New York, NY: Springer New York), 1–9

- Kolmogorov, A. N. 1991, Proceedings of the Royal Society of London A: Mathematical, Physical and Engineering Sciences, 434, 15
- Kowal, G., Lazarian, A., & Beresnyak, A. 2007, *Apj*, 658, 423
- Lazarian, A. 2004, *Journal of Korean Astronomical Society*, 37, 563
- Lazarian, A. 2011, *arXiv*, 10
- Lazarian, A., & Esquivel, A. 2003, *Apjl*, 592, L37
- McDonough, J. M. 2007, *Introductory Lectures on Turbulence*, university of Kentucky
- McKee, C. F., & Ostriker, E. C. 2007, *Annual Review of Astronomy & Astrophysics*, 45, 565
- Morris/AirTeamImages, S. 2007, *Wake turbulence*
- Narayanan, G., Heyer, M. H., Brunt, C., et al. 2008, *ApJS*, 177, 341
- Ossenkopf, V. 2002, *A&A*, 391, 295
- Planck Collaboration, Ade, P. A. R., Aghanim, N., et al. 2016, *A&A*, 586, A138
- Rybicki, G. B., & Lightman, A. P. 2007, *Plasma Effects* (Wiley-VCH Verlag GmbH), 167–194;224–237
- Savage, B. D., & Mathis, J. S. 1979, *Annual Review of Astronomy & Astrophysics*, 17, 73
- Sutton, E. C. 2011, *Observational Astronomy* (Cambridge University Press), *cambridge Books Online*
- Tielens, A. G. G. M. 2005, *The Physics and Chemistry of the Interstellar Medium* (Cambridge University Press), *cambridge Books Online*
- Trippe, S. 2014, *Journal of Korean Astronomical Society*, 47, 15

Vazquez-Semadeni, E. 2012, 72, 43

Very Large Telescope image, E. M. 2011, Superbubble LHA 120-N44 in the LMC

Wayfarer, S. 2016, Waikato River rapids, solo Wayfarer

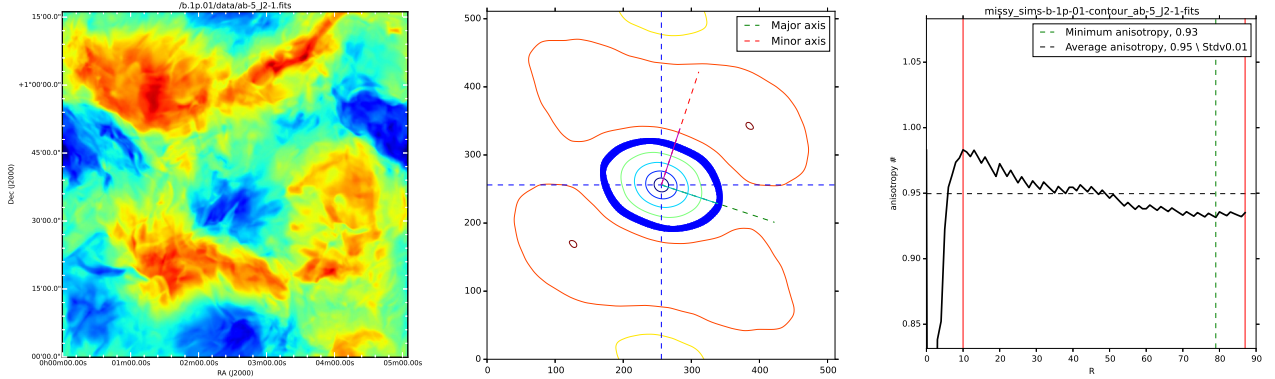
Werne, D. J. 2016, Turbulent, boulder/CoRA

Wikimedia Commons, B. M. 2006, a wire-grid polarizer

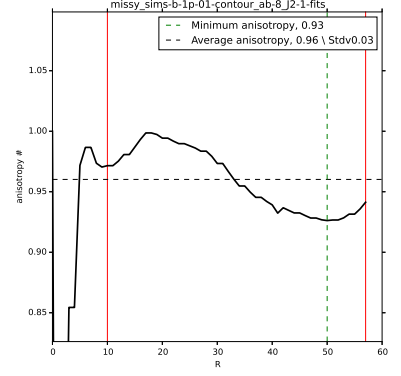
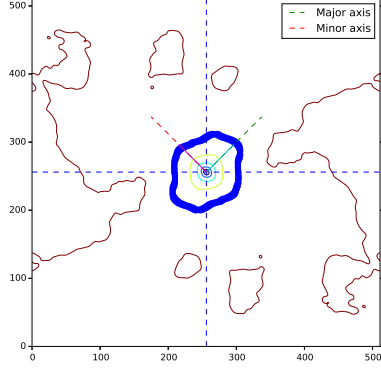
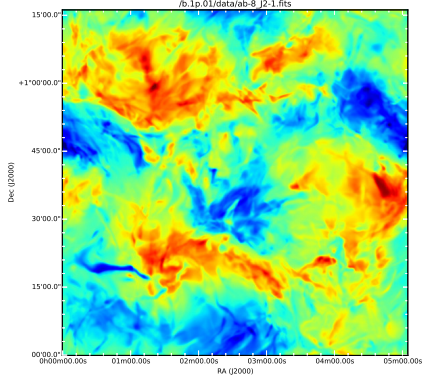
—. 2007, Faraday effect diagram

Appendix

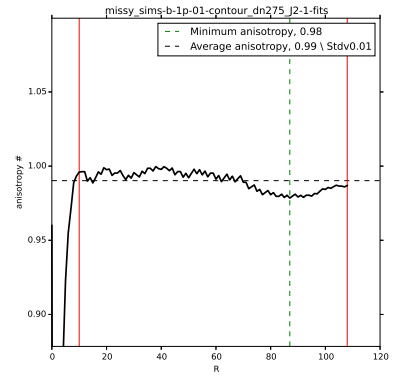
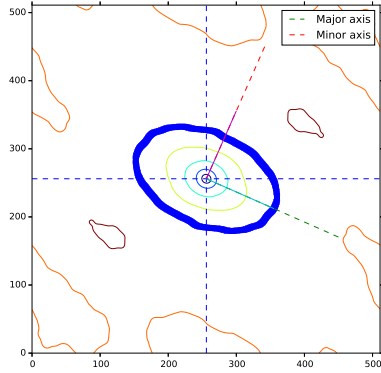
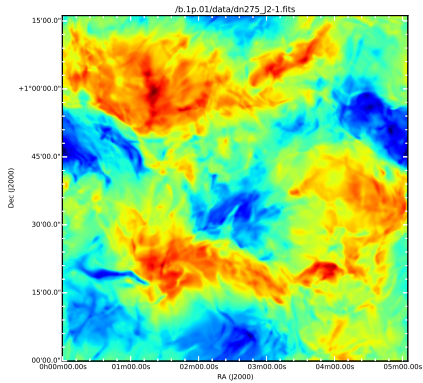
Fig. 16.—: MHD Radiative Transfer Simulations for increasing magnetic field values and pressures and various density and abundance values (which alter the opacity). Corresponding structure function contour plots and anisotropy versus scale are displayed. The axes of the moment maps and structure function plots are in pixels. The axes of the anisotropy versus scale are simply the anisotropy index and distance from the contour center.



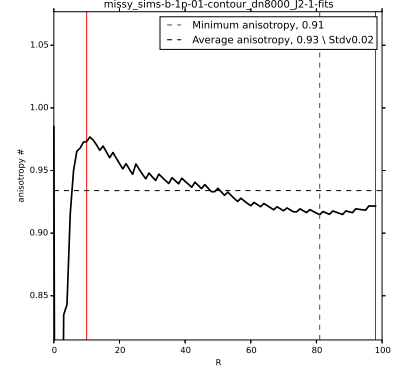
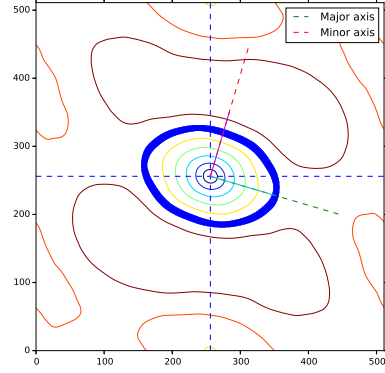
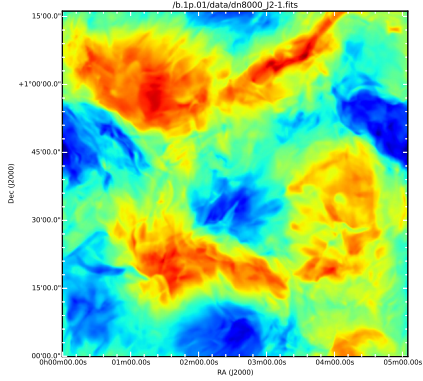
(a) $B = 0.1$ $P = 0.01$ $ab=5$



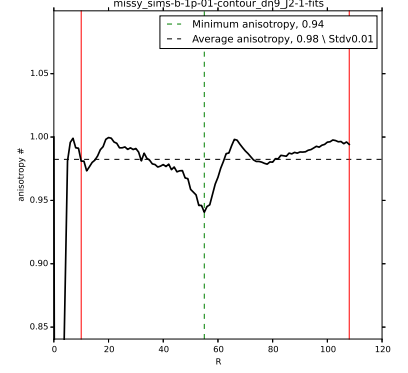
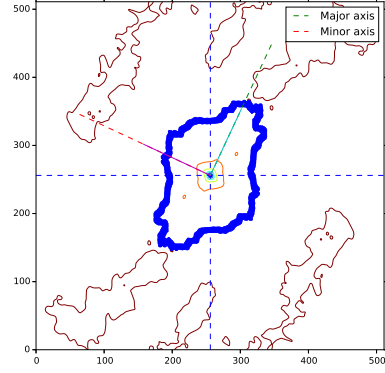
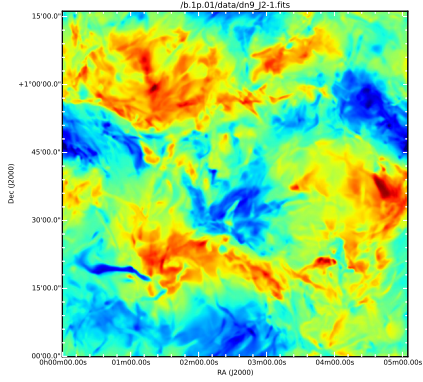
(b) $B = 0.1$ $P = 0.01$ $ab=8$



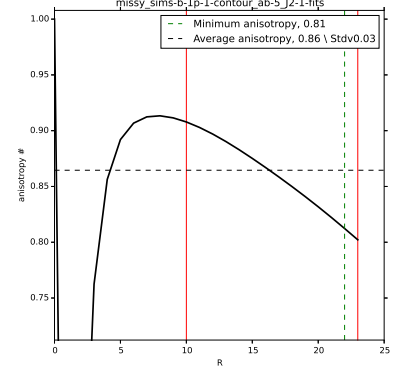
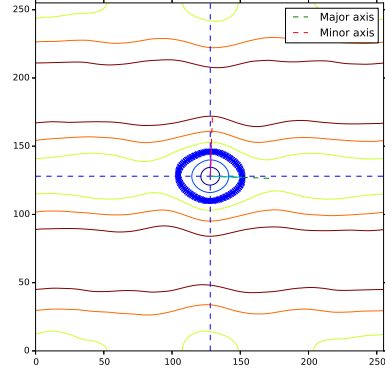
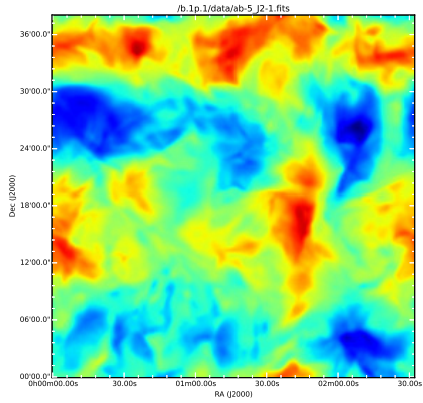
(c) $B = 0.1$ $P = 0.01$ $dn=275$



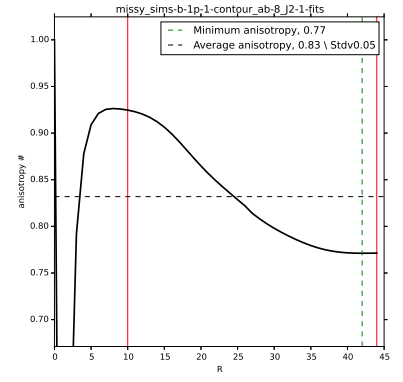
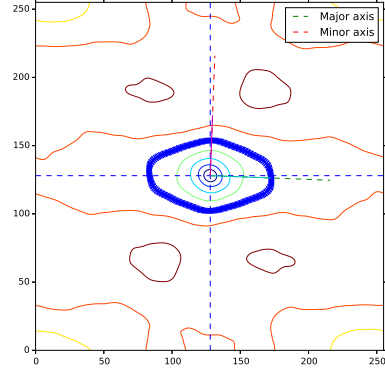
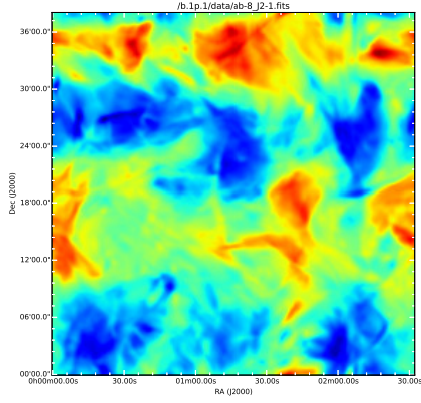
(d) $B = 0.1$ $P = 0.01$ $dn=8000$



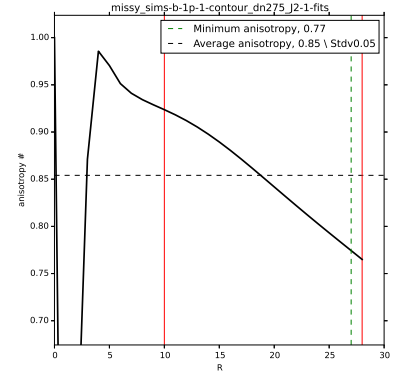
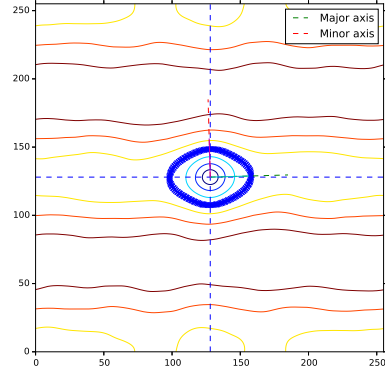
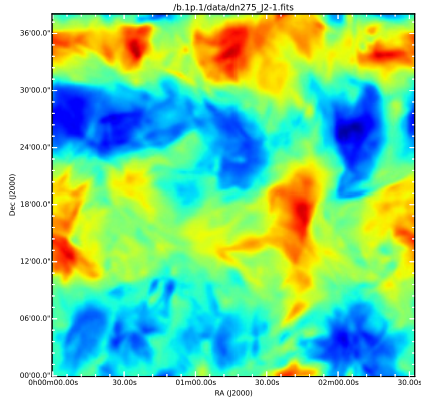
(e) $B = 0.1$ $P = 0.01$ $dn=9$



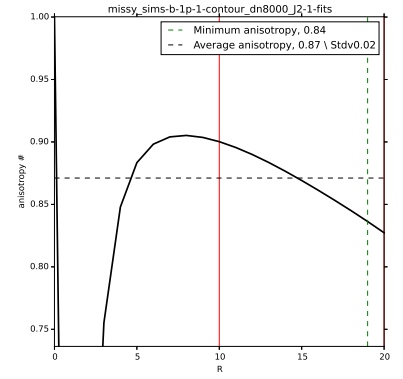
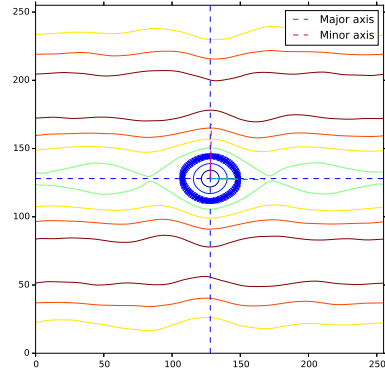
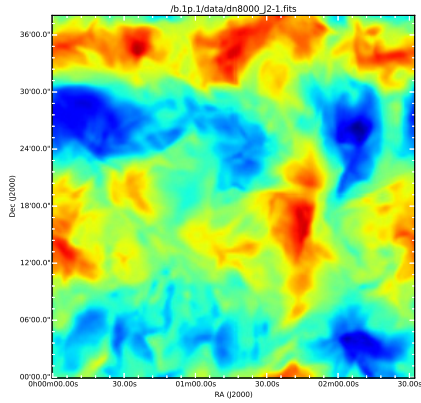
(f) $B = 0.1$ $P = 0.1$ $ab=5$



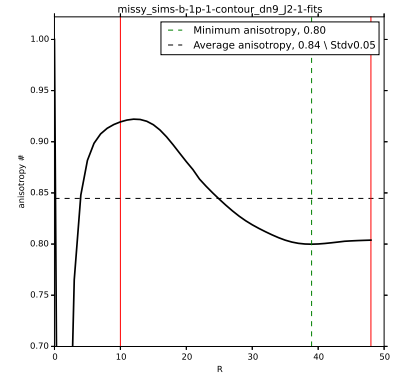
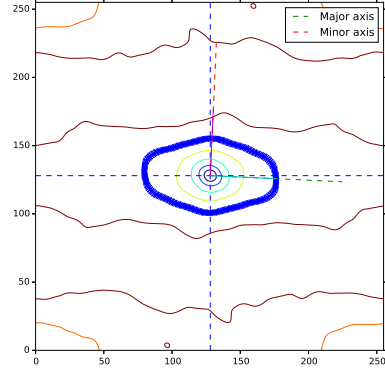
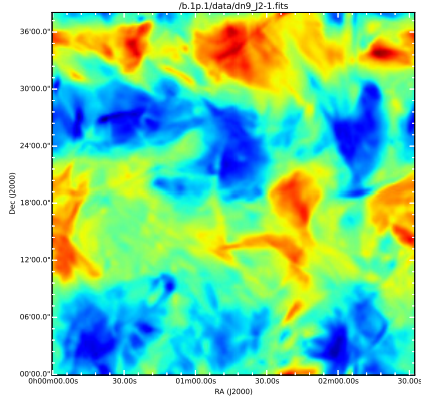
(g) $B = 0.1$ $P = 0.1$ $ab=8$



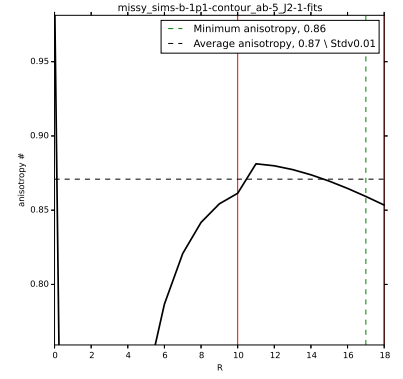
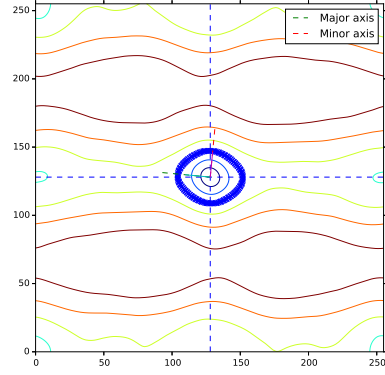
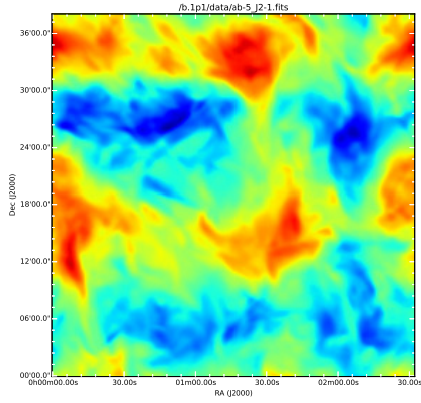
(h) $B = 0.1$ $P = 0.1$ $dn=275$



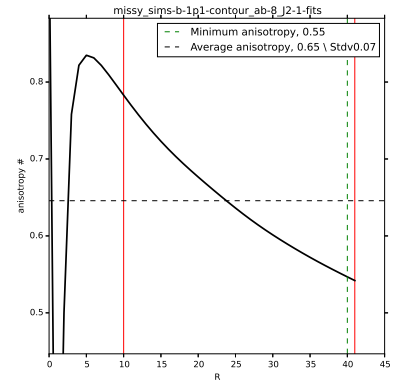
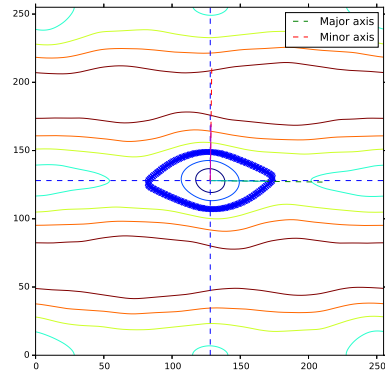
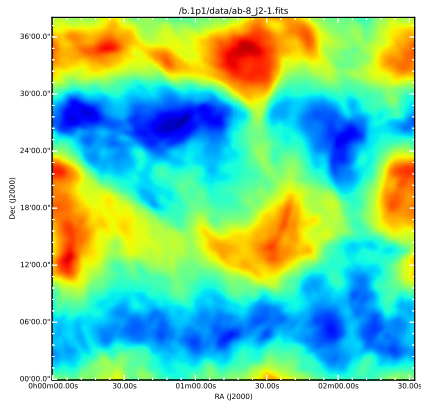
(i) $B = 0.1$ $P = 0.1$ $dn=8000$



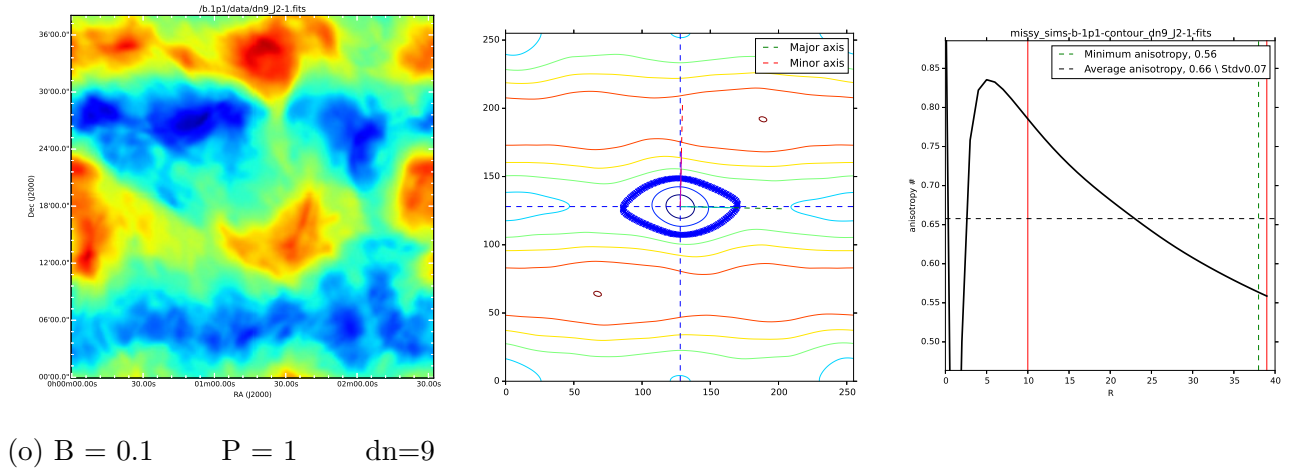
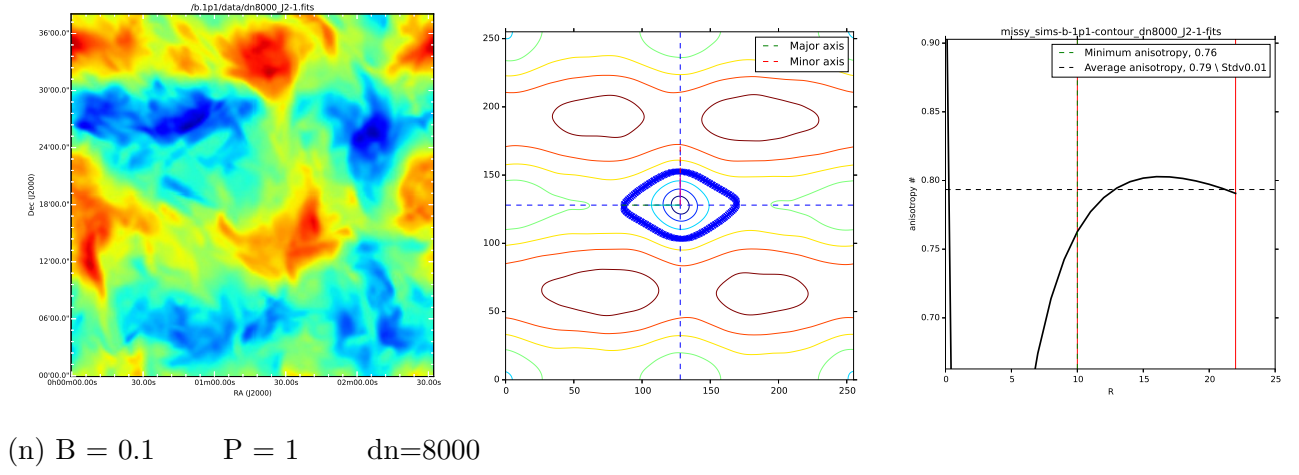
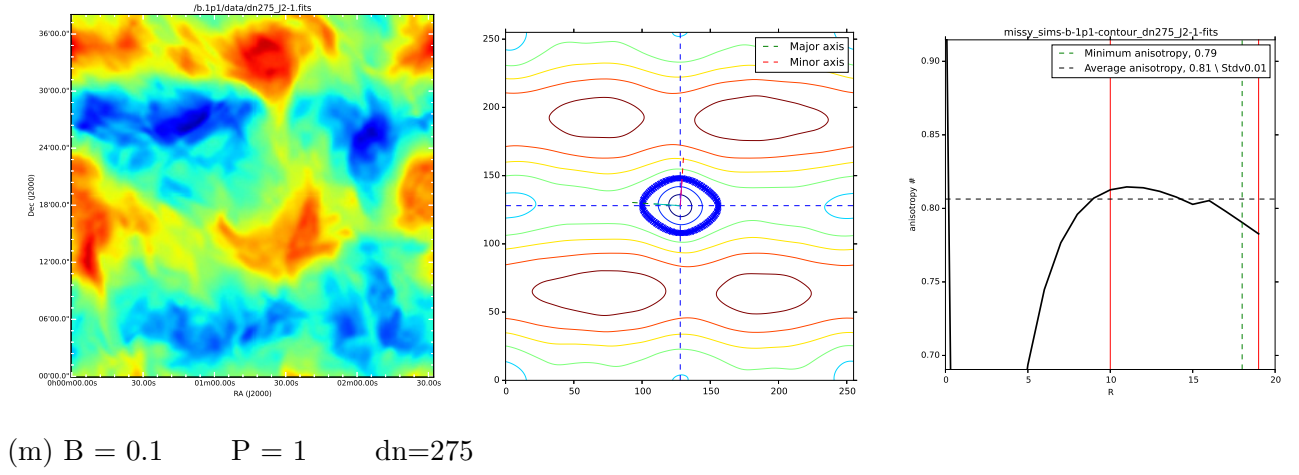
(j) $B = 0.1$ $P = 0.1$ $dn=9$

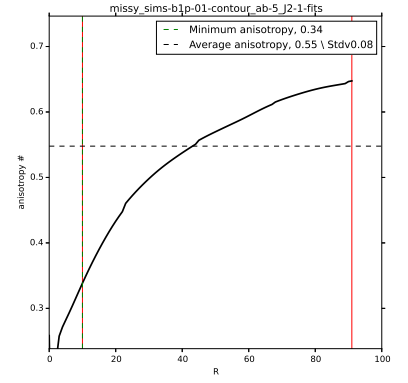
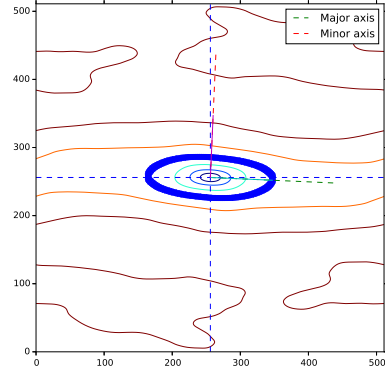
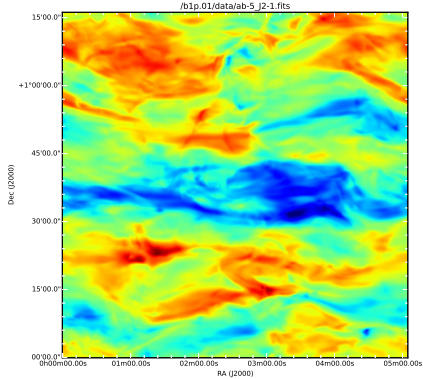


(k) $B = 0.1$ $P = 1$ $ab=5$

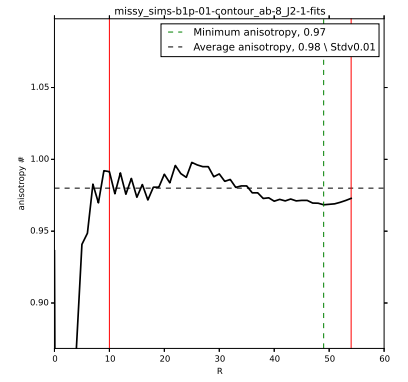
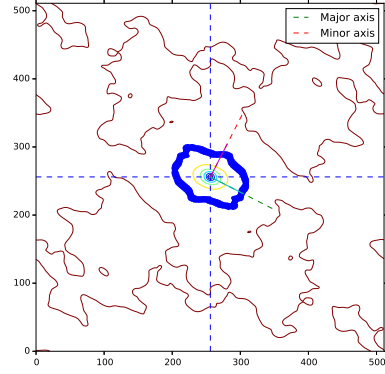
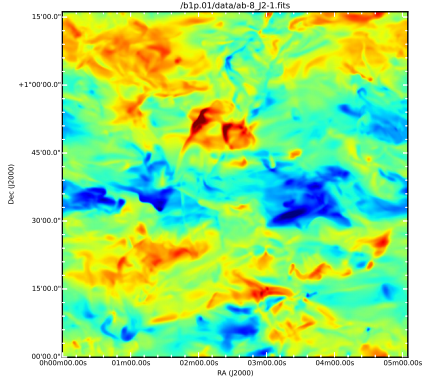


(l) $B = 0.1$ $P = 1$ $ab=8$

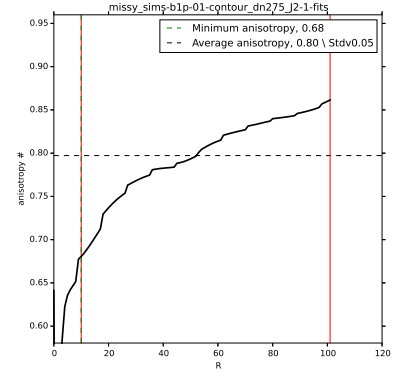
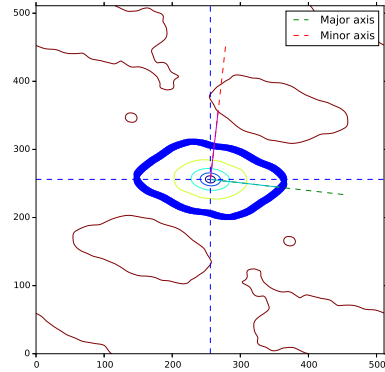
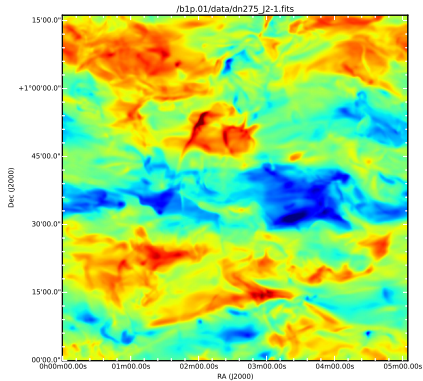




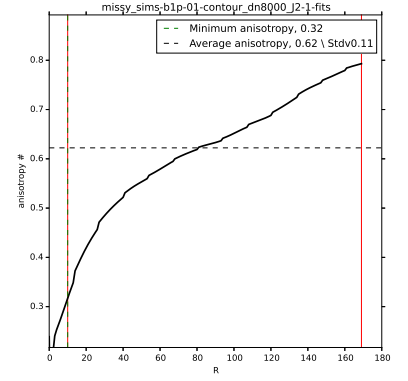
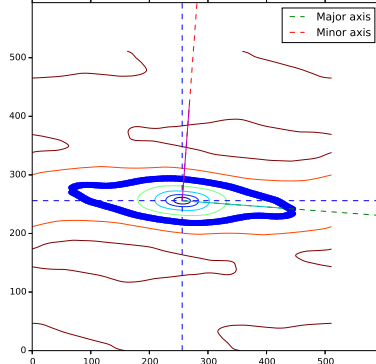
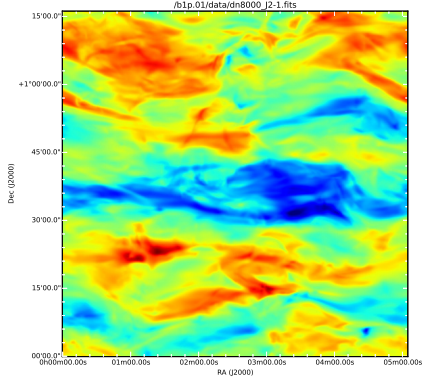
(p) $B = 1$ $P = 0.01$ $ab=5$



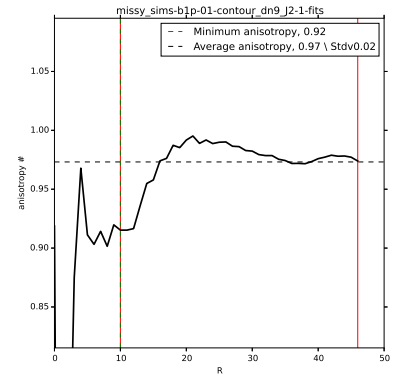
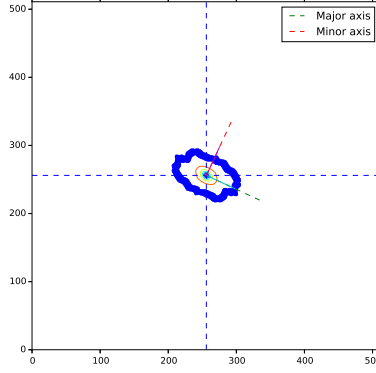
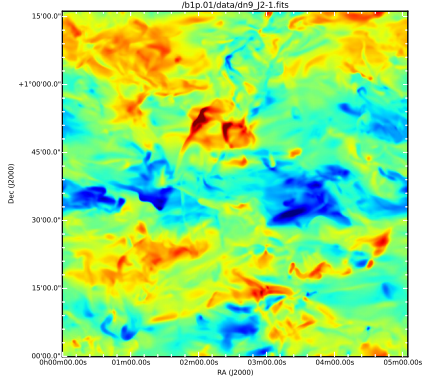
(q) $B = 1$ $P = 0.01$ $ab=8$



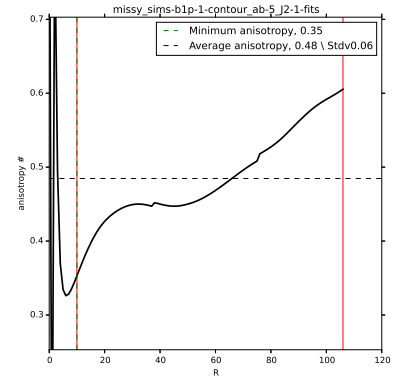
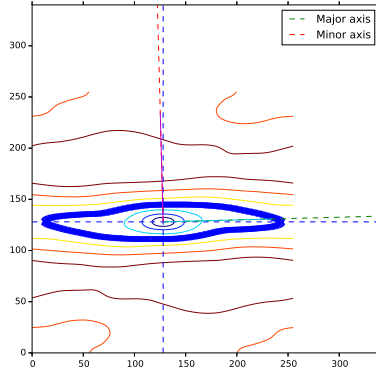
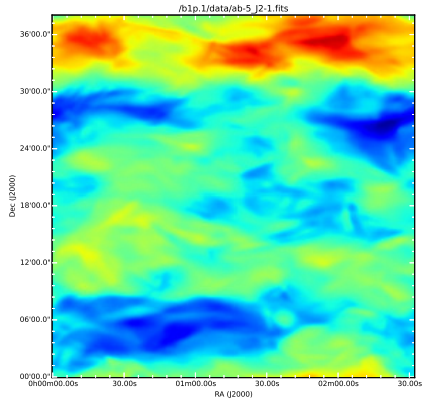
(r) $B = 1$ $P = 0.01$ $dn=275$



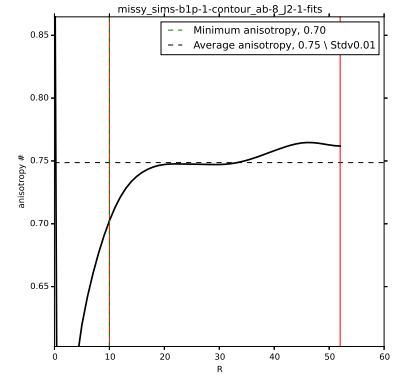
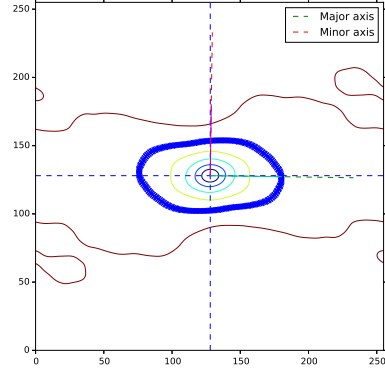
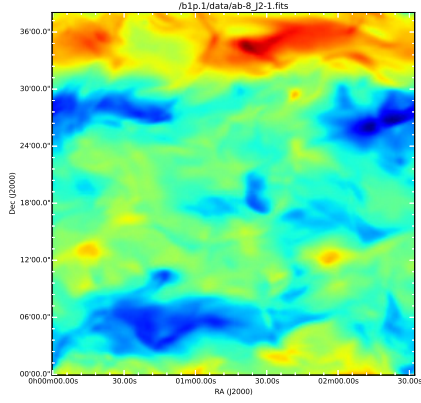
(s) $B = 1$ $P = 0.01$ $dn=8000$



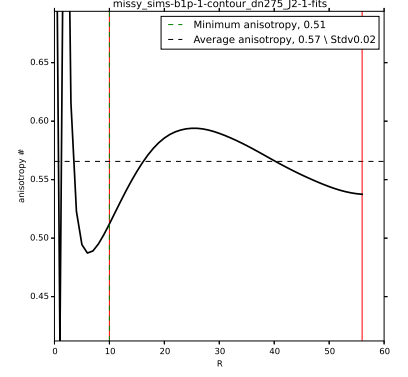
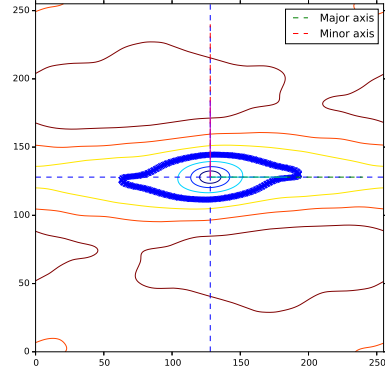
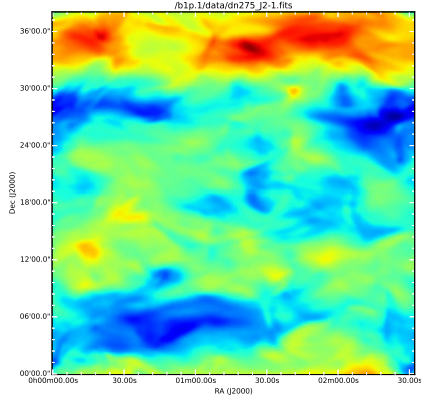
(t) $B = 1$ $P = 0.01$ $dn=9$



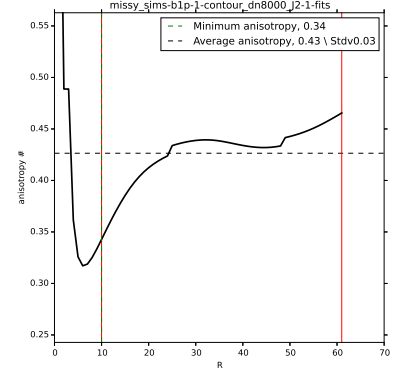
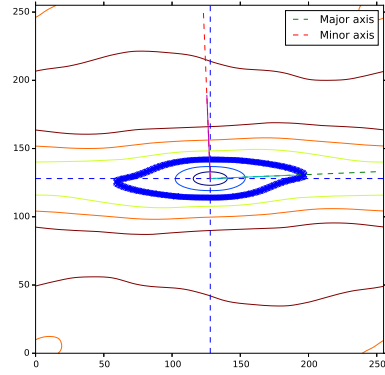
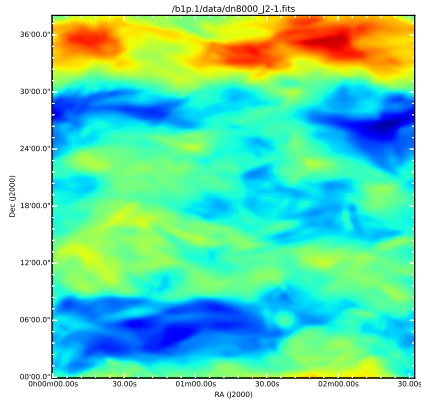
(u) $B = 1$ $P = 0.1$ $ab=5$



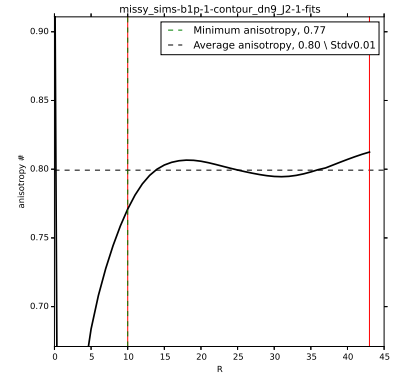
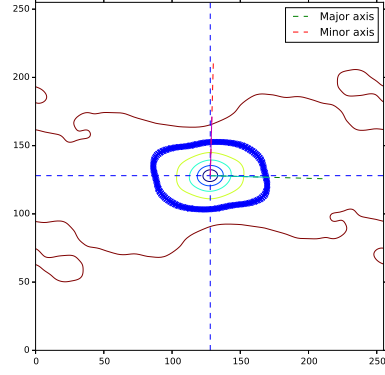
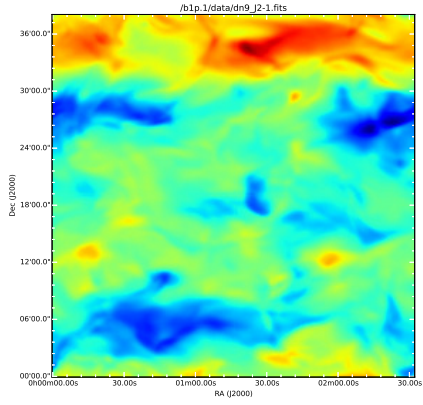
(v) $B = 1$ $P = 0.1$ $ab=8$



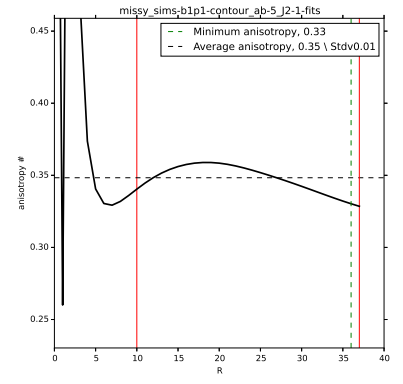
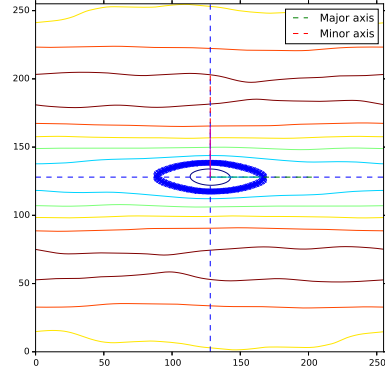
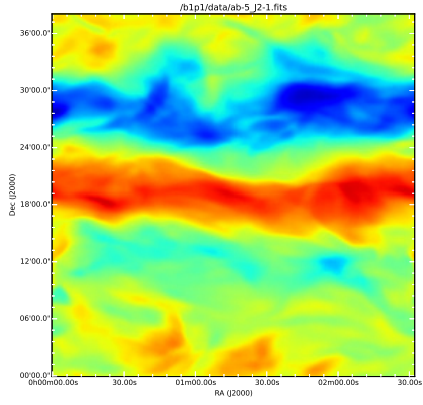
(w) $B = 1$ $P = 0.1$ $dn=275$



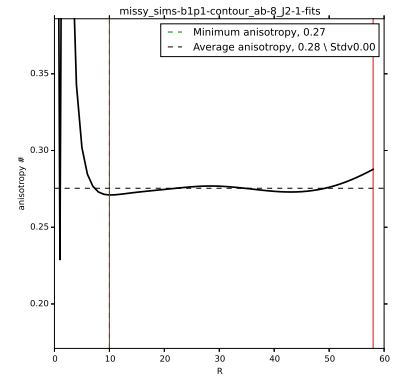
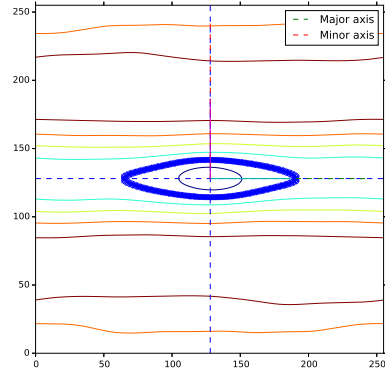
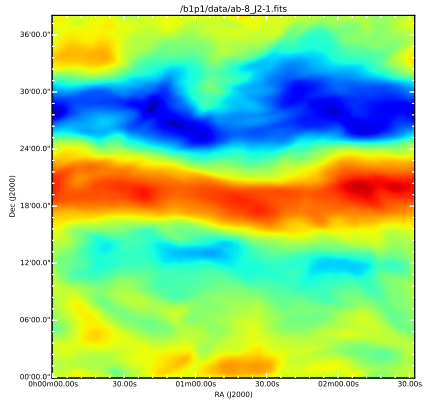
(x) $B = 1$ $P = 0.1$ $dn=8000$



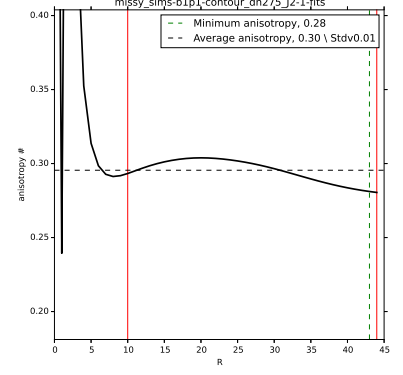
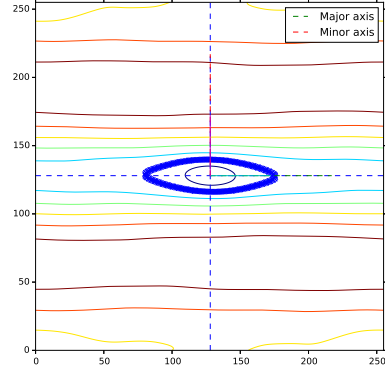
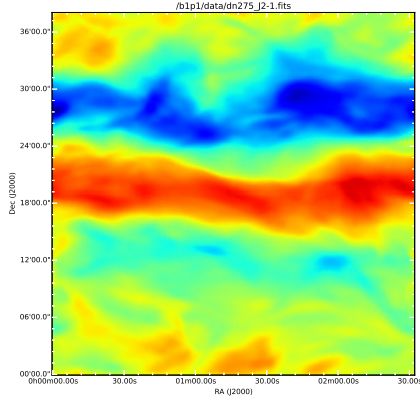
(y) B = 1 P = 0.1 dn=9



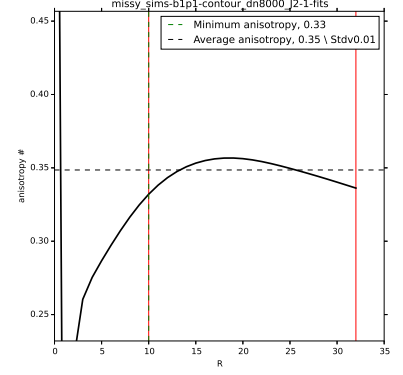
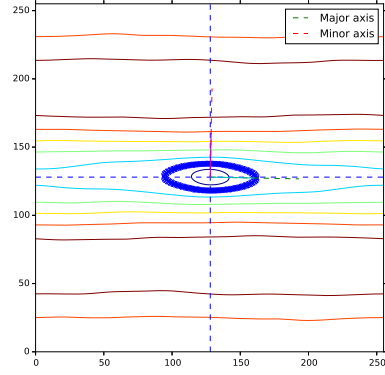
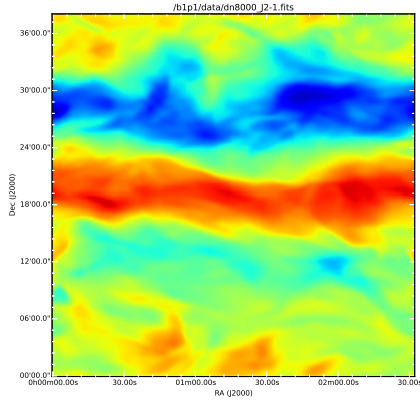
(z) B = 1 P = 1 ab=5



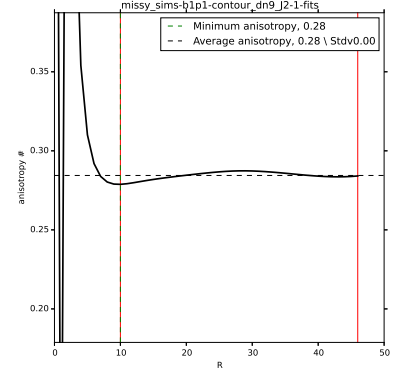
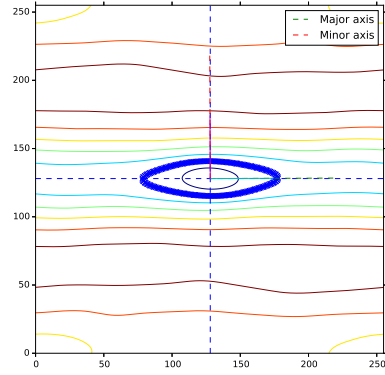
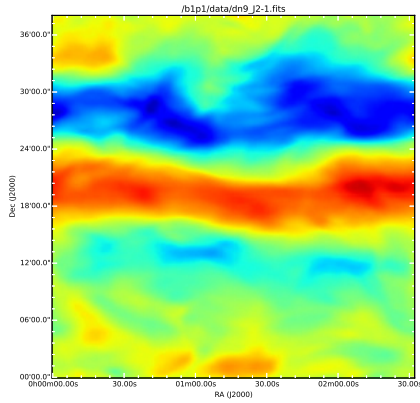
(aa) B = 1 P = 1 ab=8



(ab) $B = 1$ $P = 1$ $dn=275$

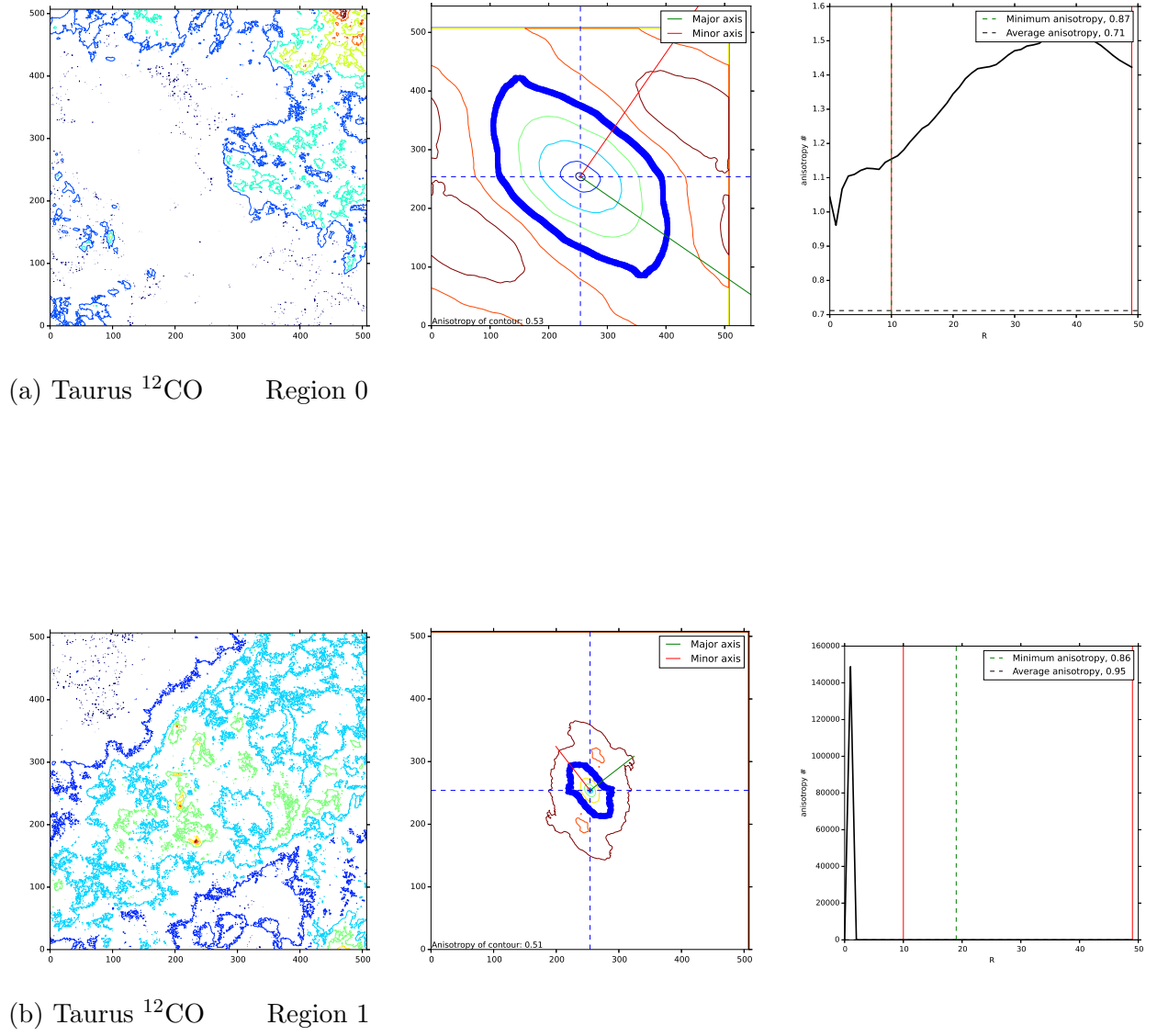


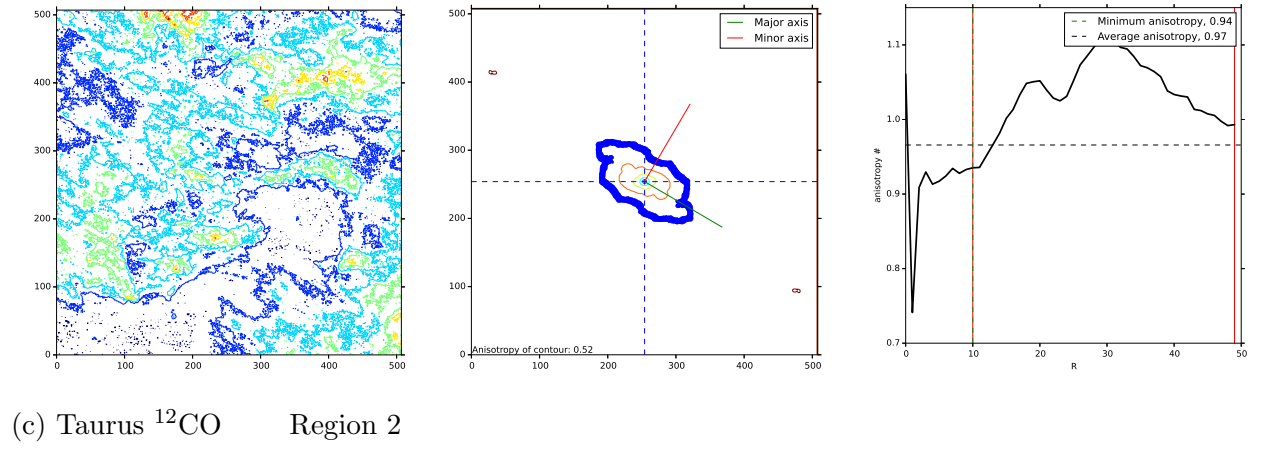
(ac) $B = 1$ $P = 1$ $dn=8000$

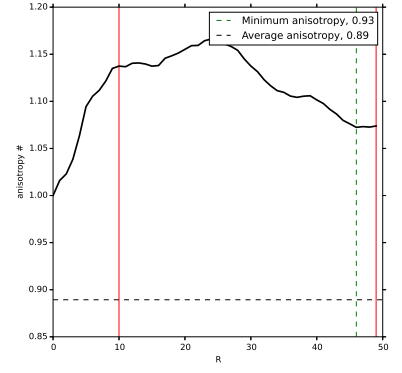
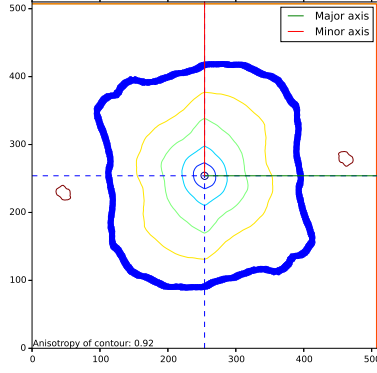
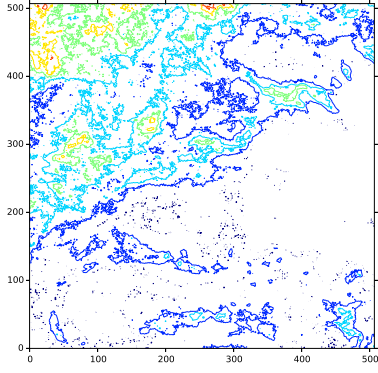


(ad) $B = 1$ $P = 1$ $dn=9$

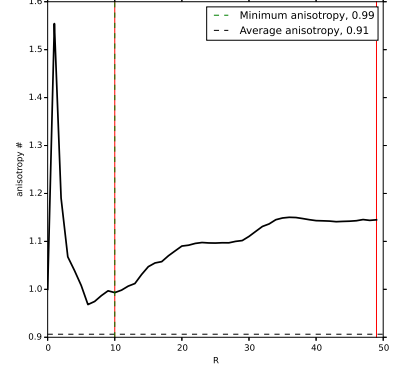
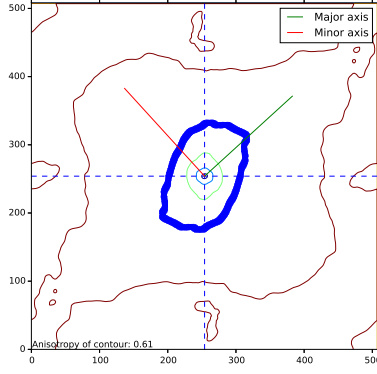
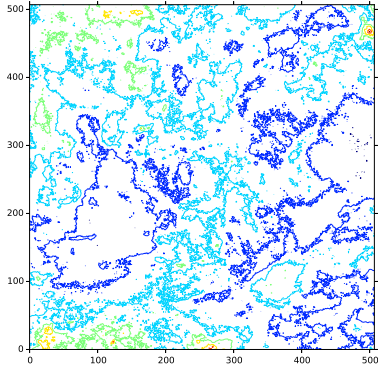
Fig. 18.—: Taurus ^{12}CO and ^{13}CO emission moment maps and their corresponding structure function contour and anisotropy versus scale plots. The axes of the moment maps and structure function plots are in pixels. The axes of the anisotropy versus scale are simply the anisotropy index and distance from the contour center.



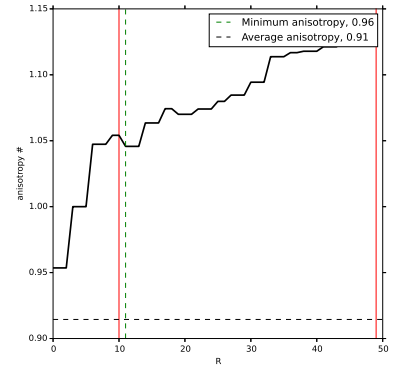
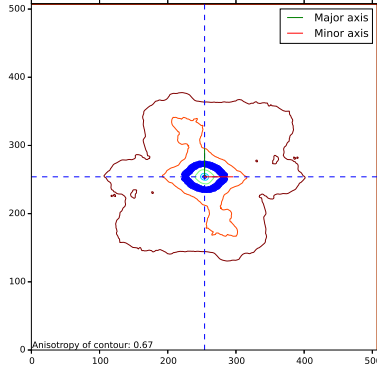
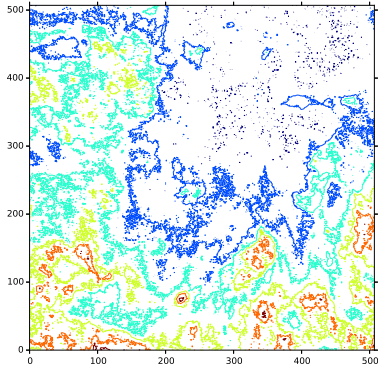




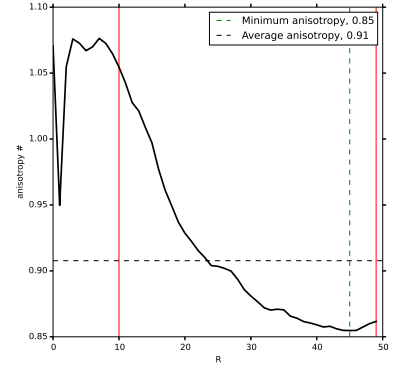
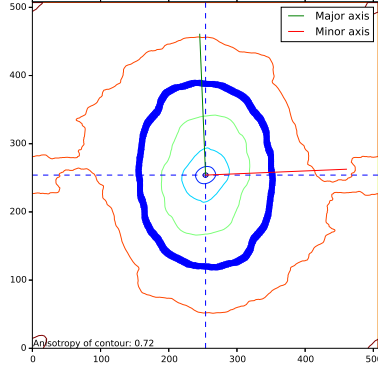
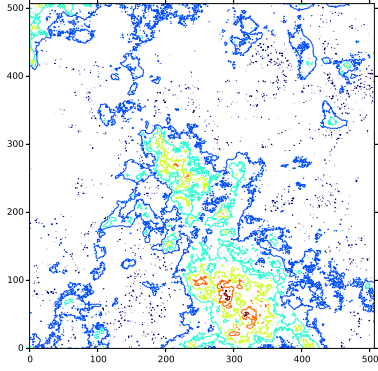
(d) Taurus ^{12}CO Region 3



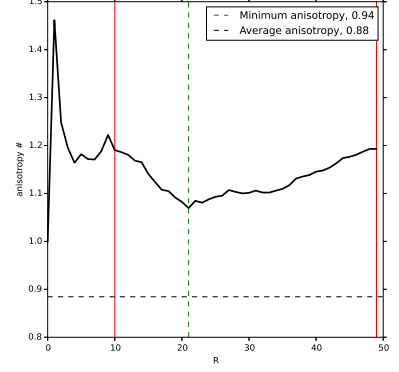
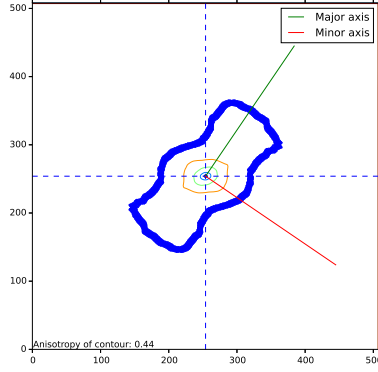
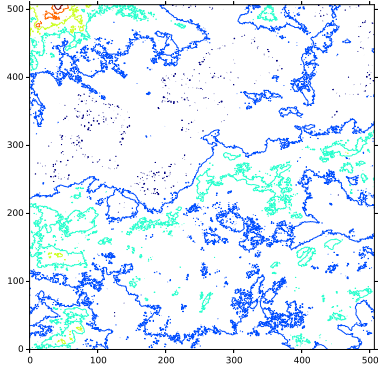
(e) Taurus ^{12}CO Region 4



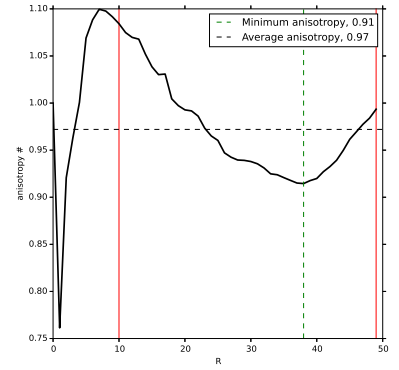
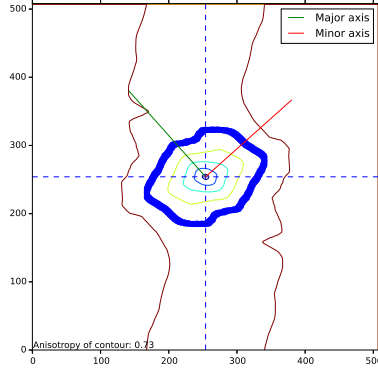
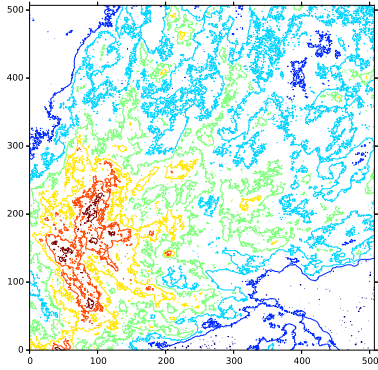
(f) Taurus ^{12}CO Region 5



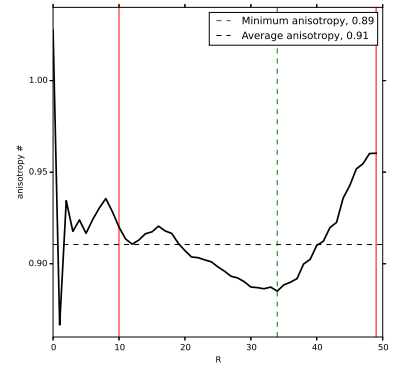
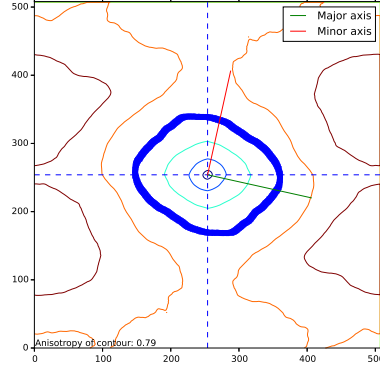
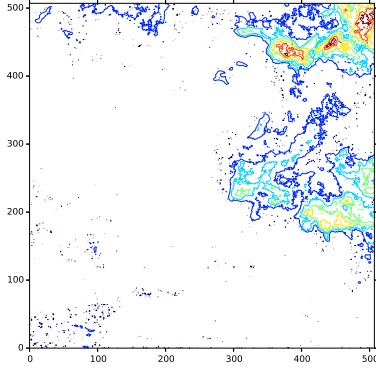
(g) Taurus ^{12}CO Region 6



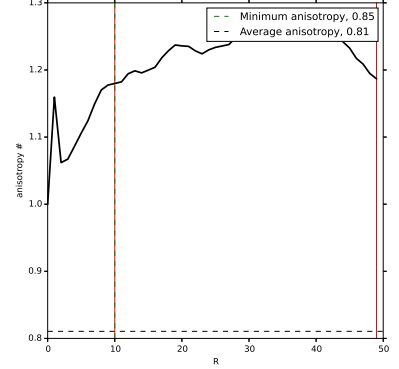
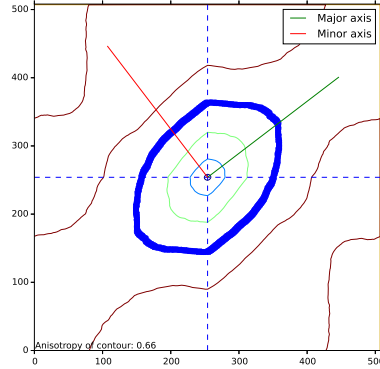
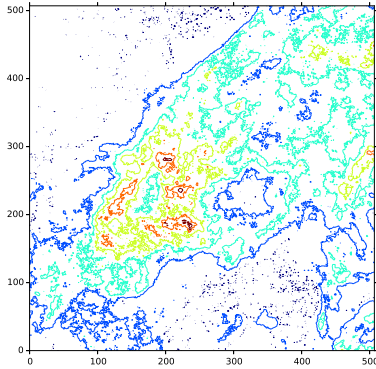
(h) Taurus ^{12}CO Region 7



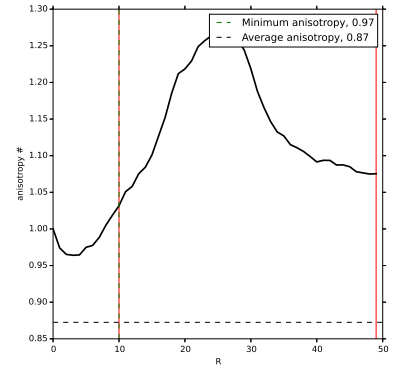
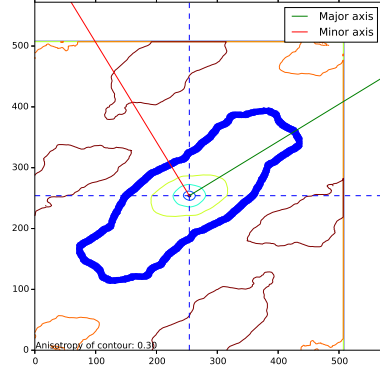
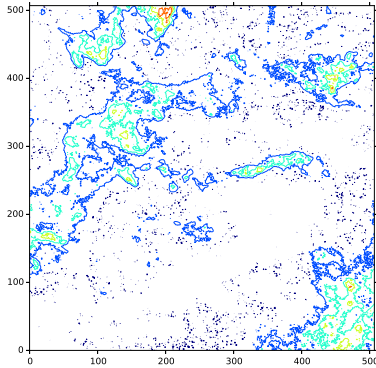
(i) Taurus ^{12}CO Region 8



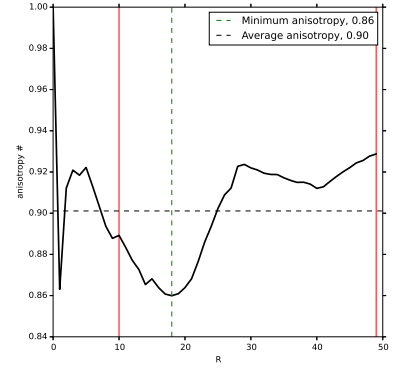
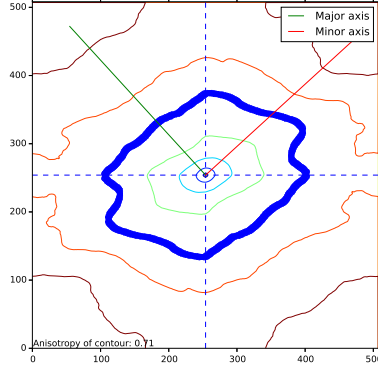
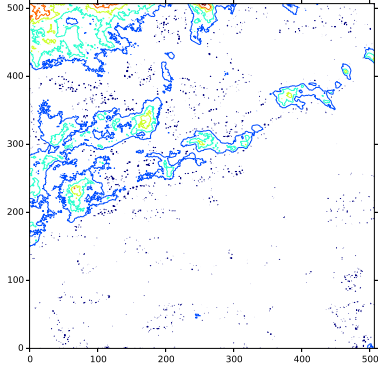
(j) Taurus ^{13}CO Region 0



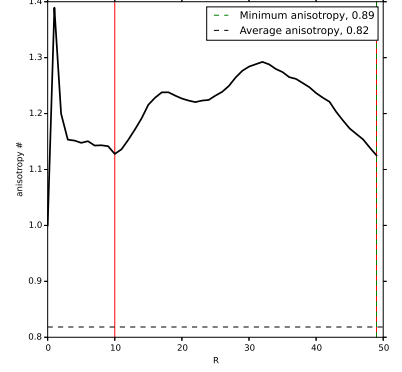
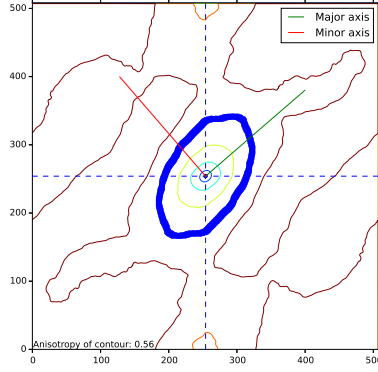
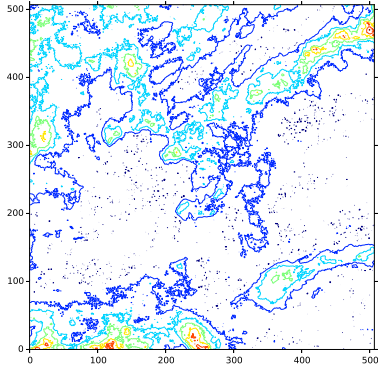
(k) Taurus ^{13}CO Region 1



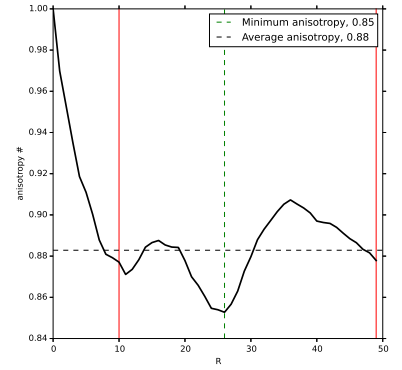
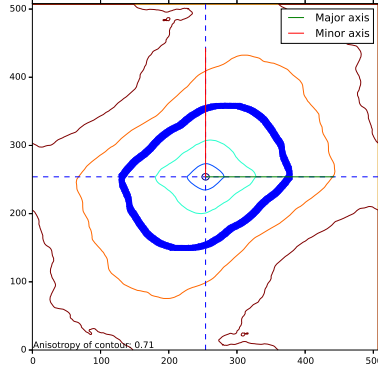
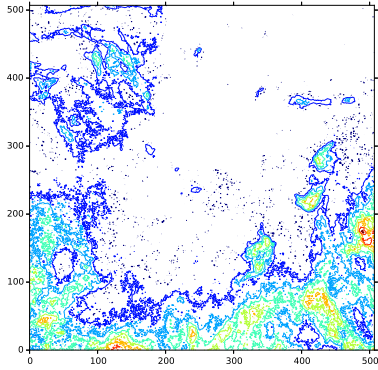
(l) Taurus ^{13}CO Region 2



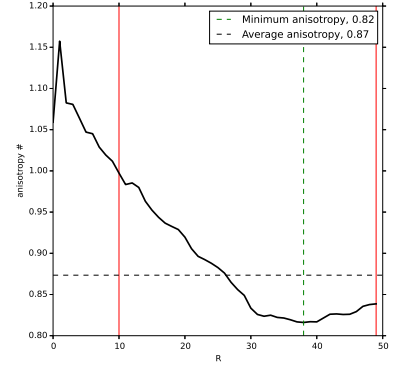
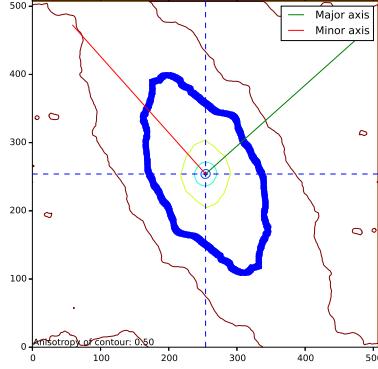
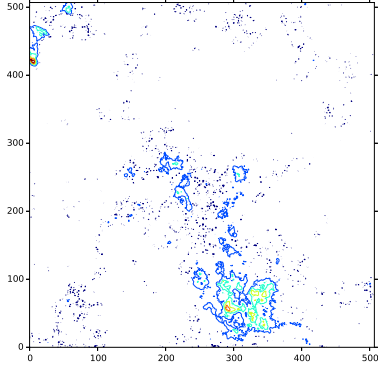
(m) Taurus ^{13}CO Region 3



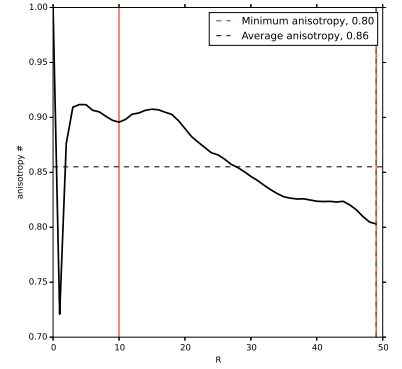
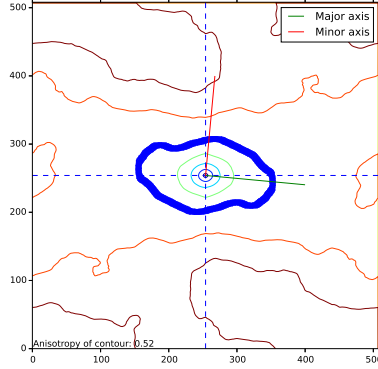
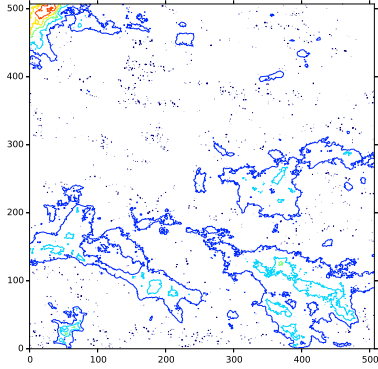
(n) Taurus ^{13}CO Region 4



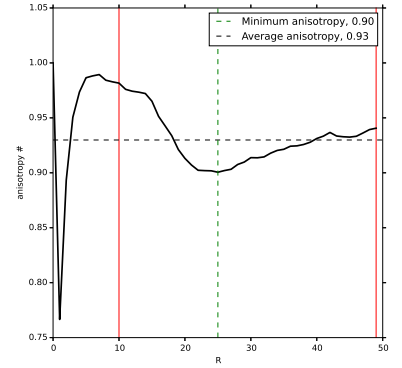
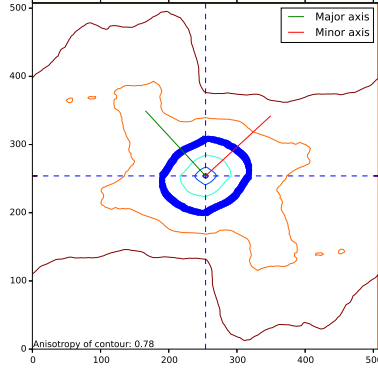
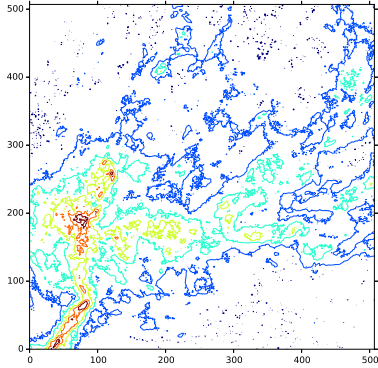
(o) Taurus ^{13}CO Region 5



(p) Taurus ^{13}CO Region 6



(q) Taurus ^{13}CO Region 7



(r) Taurus ^{13}CO Region 8